Reactive and Functional Polymers 214 (2025) 106286

Contents lists available at ScienceDirect

Reactive and Functional Polymers

journal homepage: www.elsevier.com/locate/react

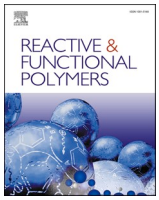

Nitrogen and sulfur co-doped microporous carbon through benzo[c]-1,2,5-thiadiazole-functionalized benzoxazine-linkage porous organic polymer in CO_2 capture and energy storage

Mohamed Gamal Mohamed [a,b,*], Chia-Chi Chen [a], Shiao-Wei Kuo [a,c,*]

[a] Department of Materials and Optoelectronic Science, Center for Functional Polymers and Supramolecular Materials, National Sun Yat-Sen University, Kaohsiung 804, Taiwan
[b] Department of Chemistry, Faculty of Science, Assiut University, Assiut 71515, Egypt
[c] Department of Medicinal and Applied Chemistry, Kaohsiung Medical University, Kaohsiung 807, Taiwan

ARTICLE INFO

Keywords:
Benzoxazine
Benzo[c]-1,2,5-thiadiazole
Porous organic polymer
Energy storage
CO_2 capture

ABSTRACT

Benzoxazine-based functional polymers have been received as promising materials because of their superior thermal stability, mechanical strength, and versatility in applications ranging from coatings to high-performance nanocomposites. In this study, we synthesized two benzo[c]-1,2,5-thiadiazole (BBT)-functionalized benzoxazine monomers: BBT-BZ and its brominated derivative, BBT-BZ-2Br, using a three-step process comprising Schiff base formation, reduction, and Mannich condensation, which were validated via FTIR, ^{1}H and ^{13}C NMR spectroscopy, and HR mass spectrometry. To further enhance functionality, the porous organic polymer (POP) was synthesized from the BBT-BZ-2Br with tetraethynylpyrene (Py-T) monomers using the Sonogashira-Hagihara coupling reaction, resulting in BBT-BZTB-Py POP. The thermal properties of the BZ monomers and their corresponding polymers were analyzed via TGA, revealing excellent thermal stability and robust cross-linked networks formed via thermal ring-opening polymerization (ROP) to create poly(BBT-BZTB-Py) POP. Subsequent carbonization of poly(BBT-BZTB-Py) POP at 600 °C with KOH activation yielded a microporous N/S co-doped carbon material, poly(BBT-BZTB-Py) POP-600. Characterization using Raman spectroscopy, XRD, XPS, and N_2 adsorption/desorption analysis confirmed the successful incorporation of heteroatoms and the development of a hierarchical microporous and mesoporous structure. This material demonstrated potential for gas capture and electrochemical energy storage applications. Overall, this work presents comprehensive work on the design, synthesis, and thermal behavior of functionalized benzoxazine monomers and their POP derivatives, emphasizing their versatility for advanced material applications.

1. Introduction

Atmospheric concentrations of greenhouse gases have markedly increased over the past two centuries [1]. Notably, carbon dioxide (CO_2) levels have risen from approximately 280 ppm in the pre-industrial era to over 420 ppm by 2023, reflecting a substantial anthropogenic influence on the global carbon cycle [2,3]. CO_2 emissions into the atmosphere vary significantly depending on the type of fuel utilized and the specific conditions under which it is processed [4]. Gas purification has emerged as a critical global challenge in response to escalating air pollution, driven in large part by the rising concentration of atmospheric CO_2 [5]. Currently, three principal technologies are employed for the removal of CO_2 from industrial emission sources: membrane separation, solid sorbent adsorption, and chemical absorption using scrubbing solutions [3,6,7]. Supercapacitors (SCs) are widely recognized for their high-power density and low maintenance requirements; however, their practical deployment is often constrained by limited energy density. Enhancing energy storage performance while retaining rapid charge–discharge capabilities require the strategic selection of advanced electrode materials [8–10]. Heteroatom doping represents an effective strategy for enhancing the specific capacitance (Cs) of supercapacitors. Incorporation of heteroatoms such as nitrogen (N), oxygen (O), boron (B), and sulfur (S) has been shown to improve surface hydrophilicity and facilitate redox interactions at the electrode–electrolyte interface

* Corresponding authors at: Department of Materials and Optoelectronic Science, Center for Functional Polymers and Supramolecular Materials, National Sun Yat-Sen University, Kaohsiung 804, Taiwan.
E-mail addresses: magamal.eldin34@gmail.com, mgamal.eldin12@aun.edu.eg (M.G. Mohamed), kuosw@faculty.nsysu.edu.tw (S.-W. Kuo).

https://doi.org/10.1016/j.reactfunctpolym.2025.106286
Received 9 February 2025; Received in revised form 30 March 2025; Accepted 31 March 2025
Available online 1 April 2025

through electron donation mechanisms [11,12].

Benzoxazine (BZ)-functionalized polymers are produced through Mannich condensation reactions involving primary amines, aromatic phenols, and formaldehyde [13–15]. These polymers have recently garnered significant attention. The ring-opening polymerization (ROP) of polybenzoxazines converts BZ monomers into thermosetting polymers via thermal curing [16–19]. As an innovative type of thermosetting resin derived from conventional phenolic resins, polybenzoxazines (PBZs) are characterized by distinctive cross-linked networks formed through phenolic Mannich bridges [20]. The strong hydrogen bonding—both within and between molecules—between phenolic groups and other functional groups, such as amines, ethers, alcohols, or aromatic rings, is pivotal in defining the properties of PBZs networks [21,22]. These interactions greatly improve their physical and chemical performance, making them highly appealing for both academic research and industrial applications. PBZs possess a wide array of remarkable properties, including exceptional thermal stability, high flame resistance, superior electrical insulation, minimal shrinkage during curing, excellent adhesion, and low water absorption [21,22]. These unique attributes are attributed to the extensive design flexibility of BZ molecules, which enables the synthesis of a variety of resins from diverse starting materials. This adaptability allows researchers to fine-tune specific characteristics to meet the demands of specialized applications, broadening the potential uses of PBZs across different industries [23–25]. Porous organic polymers (POPs) [including conjugated microporous polymers (CMPs) and covalent organic frameworks (COFs)] with high surface area and microporous characteristics could be used in energy storage, chemical sensing, hydrogen (H_2) evolution, and gas capture [26–30]. Various functionalities, including triazine, imine, imide, azine, and boroxine, have been synthesized by various Schiff base formations, Sonogashira–Hagihara couplings, and organic reactions such as cyclotrimerization, Suzuki coupling, and Suzuki coupling [28–35]. Adding new chemical bonds to POPs can expand their range of polymeric frameworks with high surface area and their possible applications [36–38]. Therefore, the challenge of preparing new benzoxazine-linkage POPs with high surface area and pore volume has recently gained significant interest. For instance, we first reported a new benzoxazine linkage POP based on 1,3,5-tris(4-aminophenyl)triazine (TAPT) unit by using Mannich condensation, which exhibited SA_{BET} of ca. 70 $m^2\ g^{-1}$ [39]. The other possible approach to forming new benzoxazine-linkage POPs is synthesized from the multistep post-modifications of imine-POPs. For example, Yaghi et al. proposed the carbamate and thiocarbamate-linked COFs through the post-modifications of imine-COFs in the solid-state chemical transformation with a surface area $> 700\ m^2\ g^{-1}$ [40]. Therefore, Ma et al. used the reduction and Mannich condensation, which employed benzoxazine-linked COF materials, featured a surface area $> 650\ m^2\ g^{-1}$ by using TAPT and dihydroxynaphthalene-1,5-dicarbaldehyde (DHNDA) as the monomers [41]. Recently, we proposed various benzoxazine-linked POPs with high surface area (100–300 $m^2\ g^{-1}$) by utilizing Sonogashira-Hagihara coupling, and various building monomers can be designed. Consequently, the ethynyl-functionalized building blocks should be paired with the brominated benzoxazine compound [38,42–46]. BBT-based materials are gaining attention for applications in gas adsorption, separation, photocatalysis, electrocatalysis, fluorescence sensitivity, and selectivity [47–50]. BBT units are key components in CMPs, and COFs for energy storage and photocatalysis were reported [51,52]. To the best of our knowledge, the primary objective is to develop BBT-functionalized BZ and its corresponding POP to investigate the influence of the BBT moiety on gas capture and supercapacitor performance. Furthermore, the insertion of heteroatoms such as nitrogen, oxygen, sulfur, and bromine into the benzoxazine monomers has proven to enhance properties such as thermal stability, flame retardancy, and surface property, further elevating the performance of these polybenzoxazines. In this work, we propose the preparation, characterization, and thermal ROP behavior of two benzo[c]-1,2,5-thiadiazole-functionalized benzoxazine monomers: BBT-BZ and its brominated derivative, BBT-BZ-2Br. Both BZ monomers were synthesized through a three-step mechanism, involving a Schiff base reaction, reduction, and the Mannich condensation. The chemical structural characteristics of these monomers were extensively studied using FTIR, ^1H, and ^{13}C NMR spectroscopy, and mass spectrometry to confirm their successful synthesis and high purity. The resulting material, BBT-BZTB-Py POP was prepared through a Sonogashira-Hagihara coupling reaction by using BBT-BZ-2Br and Py-T as starting monomers. We further investigated the thermal ROP behavior of these monomers and polymers, revealing their ability to form stable, cross-linked networks at elevated temperatures. Finally, we carbonized poly(BBT-BZTB-Py) POP at 600 °C using the KOH activation method to produce poly(BBT-BZTB-Py) POP-600, a microporous N/S co-doped microporous carbon with potential applications in gas capture and electrochemical energy storage. This work highlights the potential of functionalized benzoxazine monomers and their derivatives for use in advanced polymeric materials, offering insights into their synthesis, thermal behavior, and structural evolution under thermal and chemical modifications.

2. Experimental section

2.1. Materials

Acetone, 1,4-dioxane, sodium carbonate (Na_2CO_3), and magnesium sulfate ($MgSO_4$), hydrochloric acid (HCl), acetic acid (AcOH), 4-aminophenyl boronic acid pinacol ester, 4-bromosalicylaldehyde, copper(I) iodide (CuI, 98 %), *N*,*N*-dimethylacetamide (DMAc), *N*,*N*-dimethylformamide (DMF), ethanol (EtOH), methanol (MeOH), $Pd(PPh_3)_4$, salicylaldehyde (98 %), sodium borohydride ($NaBH_4$), tetrahydrofuran (THF), toluene, triethylamine (Et_3N), and triphenylphosphine (PPh_3, 99 %) were purchased from Sigma-Aldrich, Acros Organics and Aencore. Tetraethynylpyrene (Py-T) was synthesized following our previous procedures [42,43]. Detailed synthetic procedures for BBT-SF, BBT-Red, BBT-SF-2Br, and BBT-Red-2Br are described in the Supplementary Information.

2.2. Synthesis of BBT-2NH$_2$

4-Aminophenylboronic acid pinacol ester (1.50 g, 6.80 mmol), 4,7-dibromobenzo[c]-1,2,5-thiadiazole [53,54] (1.00 g, 3.40 mmol), Na_2CO_3 (1.27 g, 11.20 mmol), $Pd(PPh_3)_4$ (0.196 g, 0.169 mmol), H_2O (12 mL), and toluene (80 mL) were injected to a 100 mL single-neck bottle, heated to 75 °C under an N_2 atmosphere, and refluxed for 36 h. The solvent was removed under reduced pressure using a rotary evaporator. The residue was subjected to liquid–liquid extraction with DCM, 2 M HCl, and water. The organic layer was separated, dried over $MgSO_4$, and filtered. The filtrate was concentrated under reduced pressure, and the resulting residue was treated with MeOH to afford BBT-2NH$_2$ as an orange powder. FTIR (KBr, cm^{-1}): 3470, 3366 (NH_2), 3036 (C=C − H). ^1H NMR (ppm): $\delta = 7.76–6.71$ (phenyl protons), 5.38 (NH_2). ^{13}C NMR (ppm): $\delta = 154.48–114.36$ (aromatic carbons).

2.3. Synthesis of BBT-BZ

BBT-Red (0.5 g, 1.0 mmol), CH_2O (0.07 g, 2.2 mmol), 1,4-dioxane (40 mL) and EtOH (20 mL) into 100 mL round-bottom flask and refluxing the mixture at 90 °C for 24 h under N_2 atmosphere, then a rotary evaporator was removed, added MeOH to filter, washed with MeOH several times and finally put it in a vacuum oven overnight to dry to obtain an orange solid (Yield: 88 %). FTIR (cm^{-1}): 1205, 956 (oxazine ring). ^1H NMR (ppm): $\delta = 7.91–6.73$ (phenyl protons), 5.53 (OCH_2N), 4.75 ($ArCH_2N$). ^{13}C NMR (ppm): $\delta = 154.71–116.89$ (aromatic carbons), 78.71 (OCH_2N), 49.03 ($ArCH_2N$). HR ES-MS (*m/z*): calcd for ($C_{34}H_{26}N_4O_2S$), 554.67; found, 555.1842.

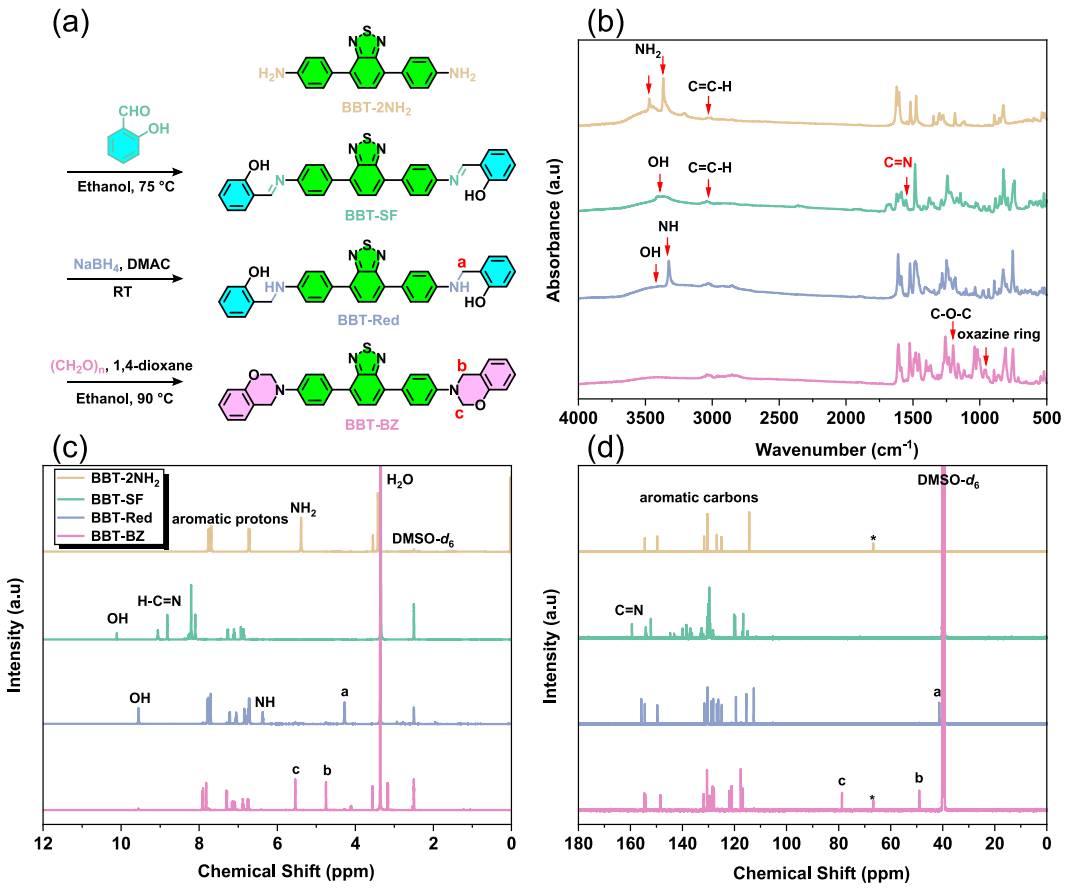

Fig. 1. (a) chemical structures and the reaction scheme, and their corresponding (b) FTIR, (c) ^{1}H NMR, and (d) ^{13}C NMR spectra of BBT-2NH$_2$, BBT-SF, BBT-Red, and BBT-BZ. (* is the 1,4-dioxane solvent).

2.4. Synthesis of BBT-BZ-2Br

BBT-Red-2Br (1.70 mmol), CH_2O (3.80 mmol), EtOH (40 mL), and 1,4-dioxane (60 mL) were injected into a 200 mL single-neck flask, and the mixture was evenly stirred at 90–100 °C under an N_2 atmosphere for 1 day. After one day, using a rotary evaporator to remove the solvents, MeOH was added to the filter, and washing with MeOH was repeated. Finally, dry it for one night in a vacuum oven to produce an orange powder with a yield of 75 %. FTIR (KBr, cm^{-1}): 1201 (C-O-C stretching), 954 (oxazine ring), 593 (C—Br). ^{1}H NMR (500 MHz, δ, ppm): δ = 7.90–6.55 (phenyl protons), 5.58 (OCH_2N), 4.73 ($ArCH_2N$). Solid state ^{13}C NMR ppm): δ = 154.05–110.47 (aromatic carbons), 78.06 (OCH_2N), 48.10 ($ArCH_2N$). HR ES-MS (m/z): calcd for ($C_{34}H_{24}Br_2N_4O_2S$), 712.46; found, 715.3211.

2.5. Synthesis of BBT-BZTB-Py POP

The synthesis of BBT-BZTB-Py POP was carried out according to the Sonogashira-Hagihara coupling reaction in the presence of BBT-BZ-2Br (0.56 mmol), Py-T (0.28 mmol), CuI (0.028 mmol), PPh_3 (0.028 mmol), and $Pd(PPh_3)_4$ (0.028 mmol) into 200 mL round bottom flask, then add Et_3N (10 mL) and DMF (10 mL) to dissolve and the mixture was kept at 90 °C for 3 days to afford brown powder with a yield of 77 % after washing by acetone, MeOH, EtOH, and THF; respectively.

2.6. Thermal Polymerization of BBT-BZ, BBT-BZ-2Br, and BBT-BZTB-Py POP

To obtain poly(BBT-BZ),poly(BBT-BZ-2Br) and poly(BBT-BZTB-Py) POP, we put BBT-BZ, BBT-BZ-2Br and BBT-BZTB-Py POP into an oven and carried out thermal ROP at 300 °C for 3 h.

2.7. Carbonization and KOH Activation of poly(BBT-BZTB-Py) POP

First, poly(BBT-BZTB-Py) POP was placed in a tube furnace, raised to 300 °C at a rate of 5 °C min^{-1} under a stable flow rate of N_2 atmosphere, and maintained for 1 h. Then increase the temperature to 600 °C at a rate of 5 °C min^{-1} and maintain for 6 h to obtain the carbonized sample. Then, mix the sample and KOH (sample/KOH weight ratio of 1), add H_2O to prepare a mixed solution (KOH concentration needs to be 3.5 M), and stir at room temperature for one day. Use a rotary evaporator to remove the water and send it to the tube furnace. Under a steady flow of N_2 atmosphere, increase to 300 °C at a rate of 5 °C min^{-1} and hold for 1 h. Finally, the temperature is raised to 600 °C at a rate of 5 °C min^{-1} and maintained for 8 h to obtain the chemically activated product, poly(BBT-BZTB-Py) POP-600.

3. Results and discussion

3.1. Characterization of the BBT-BZ monomer

The reaction scheme for the synthesis of BBT-BZ monomer used the three-step mechanism as shown in **Fig. 1(a)**. The first step was from BBT-2NH$_2$ and salicylaldehyde to perform a Schiff base reaction to obtain BBT-SF, and the second step was to reduce it to form BBT-Red with $NaBH_4$ reaction. Finally, the BBT-BZ monomer was formed by reacting with CH_2O under the Mannich condensation reaction. FTIR and NMR spectroscopy were used to identify the molecular structure of these BBT derivatives and BBT-BZ monomers, as displayed in **Figs. 1(b)-1(d)**. **Fig. 1(b)** shows the FTIR spectra of their corresponding BBT derivatives

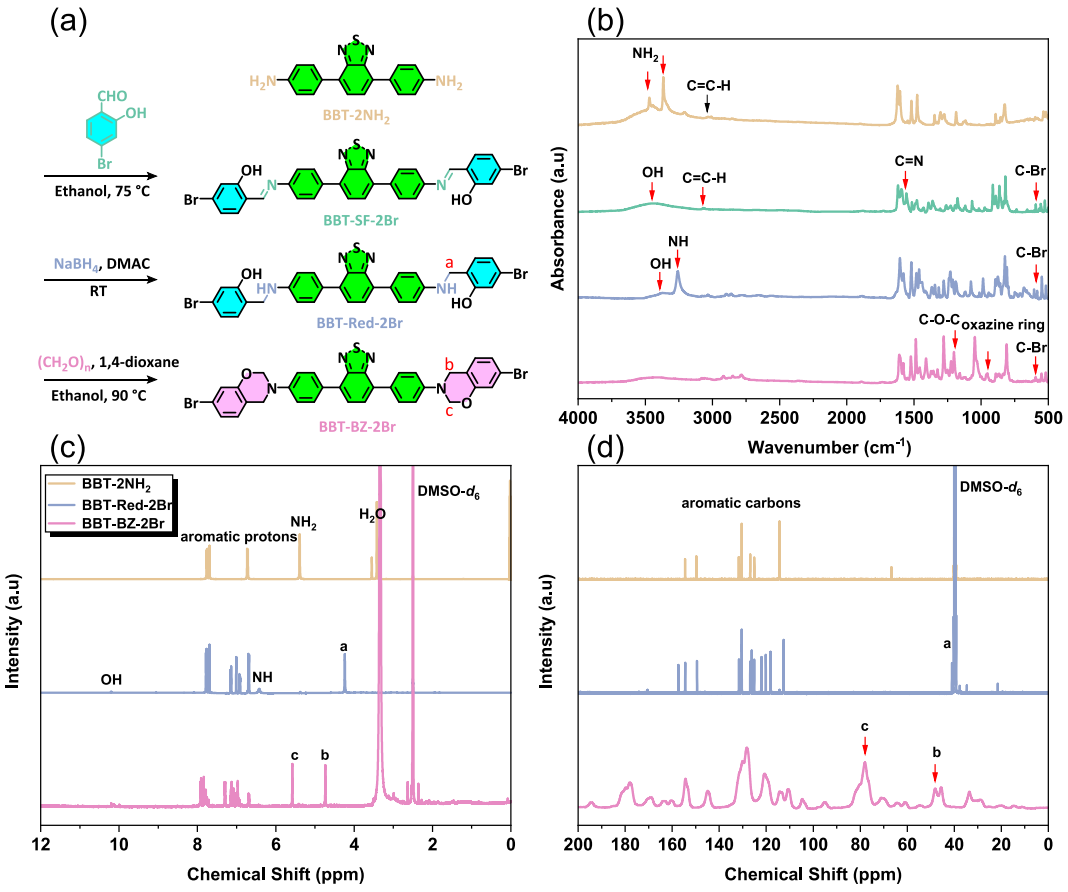

Fig. 2. (a) Schematic scheme for synthesizing BBT-BZ-2B and (b) FTIR spectra BBT-2NH_2, BBT-SF-2Br, BBT-Red-2Br, and BBT-BZ-2Br. (c) ^{1}H NMR, and (d) ^{13}C NMR spectra of BBT-2NH_2, BBT-Red-2Br, and BBT-BZ-2Br.

and BBT-BZ monomer, where the BBT-2NH_2 compound exhibited the NH_2 absorption at 3470 cm^{-1} and 3366 cm^{-1}, corresponding to asymmetric and symmetric N—H absorption, respectively, and the C=C – H absorption signal was observed at 3036 cm^{-1}. After the Schiff base reaction to form BBT-SF compound, the absorption signals representing OH, and C═N appeared at 3400 and 1552 cm^{-1}, respectively. After reduction to form the BBT-Red compound, the C═N signal disappears, and the absorption signals representing OH and NH appear at 3406 cm^{-1} (broad) and 3325 cm^{-1} (sharp), respectively. The BBT-BZ monomer was successfully prepared through the Mannich condensation method, with absorption bands at 1205 and 956 cm^{-1} attributed to C—O stretching and the oxazine ring. Furthermore, **Fig. 1(c)** shows ^{1}H NMR spectra where the BBT-2NH_2 compound has characteristic signals representing aromatic protons (7.76–6.71 ppm) and NH_2 units (5.38 ppm). After the Schiff base reaction, the BBT-SF derivative showed the characteristic signals representing OH (10.11 ppm), N=C – H (8.81 ppm), and aromatic protons (8.20–6.82 ppm). After further reduction to form the BBT-Red compound, the characteristic signals representing OH (9.55 ppm), aromatic protons (7.79–6.70 ppm), NH (6.37 ppm), and $HNCH_2$ (a, 4.28 ppm) appeared. Finally, after the Mannich condensation reaction to form BBT-BZ monomer, the obvious characteristic signals of aromatic protons (7.91–6.73 ppm), OCH_2N (c, 5.53 ppm), and $ArCH_2N$ (b, 4.75 ppm) appeared. **Fig. 1(d)** shows their corresponding ^{13}C NMR spectra, showing that the BBT-2NH_2 monomer has characteristic signals representing aromatic carbons (154.48–114.36 ppm). After the Schiff base reaction, the BBT-SF derivative has the characteristic signals representing N=C – H (159.44 ppm) and aromatic carbons (154.11–114.94 ppm). After reduction to form the BBT-Red compound, there are characteristic signals representing aromatic carbons (155.83–112.59 ppm) and $HNCH_2$ (a, 41.34 ppm). Finally, after the Mannich condensation reaction to form BBT-BZ, there are characteristic signals representing aromatic carbons (154.71–116.89 ppm), OCH_2N (c, 78.71 ppm), and $ArCH_2N$ (b, 49.03 ppm). Additionally, the molecular weight of the BBT-SF, BBT-Red, and BBT-BZ could be determined through HR ES-MS spectrum [**Figs. S1-S3 and Table S1**], which confirms that our synthetic structure has high purity characteristics, further confirming that we successfully synthesized the BBT-BZ through a three-step mechanism.

3.2. *Characterization of the BBT-BZ-2Br Monomer*

Similar to BBT-BZ monomer, we also used a three-step mechanism to prepare the BBT benzoxazine monomer with two bromine units (BBT-BZ-2Br) as displayed in Fig. 2(a), only the salicylaldehyde changes to 4-bromosalicylaldehyde and the other procedures are almost the same. Fig. 2(b) shows the BBT-SF-2Br derivative after the Schiff base reaction of BBT-2NH_2 with 4-bromosalicylaldehyde where the NH_2 unit signal from BBT-2NH_2 had disappeared, and the OH, C═N, and C—Br absorption peaks appeared at 3444, 1556, and 594 cm^{-1}, respectively. After the reduction reaction with $NaBH_4$ to provide BBT-Red-2Br compound, the C═N signal disappeared, and the absorption peaks representing OH, NH, and C—Br appeared at 3373 cm^{-1} (broad), 3258 cm^{-1} (sharp), and 582 cm^{-1}, respectively. After the final formation of BBT-BZ-2Br under Mannich condensation, the absorption peaks of C—O stretching, oxazine ring, and C—Br appeared at 1201, 954, and 593 cm^{-1}, indicating the successful formation of BBT-BZ-2Br monomer. Figs. 2(c) and 2(d) show their corresponding ^{1}H and ^{13}C NMR and no spectral signals because BBT-SF-2Br is insoluble in most typical solvents. After the reduction reaction with $NaBH_4$ to form BBT-Red-2Br, the signal representing OH (10.19 ppm), aromatic protons (7.76–6.68 ppm), NH

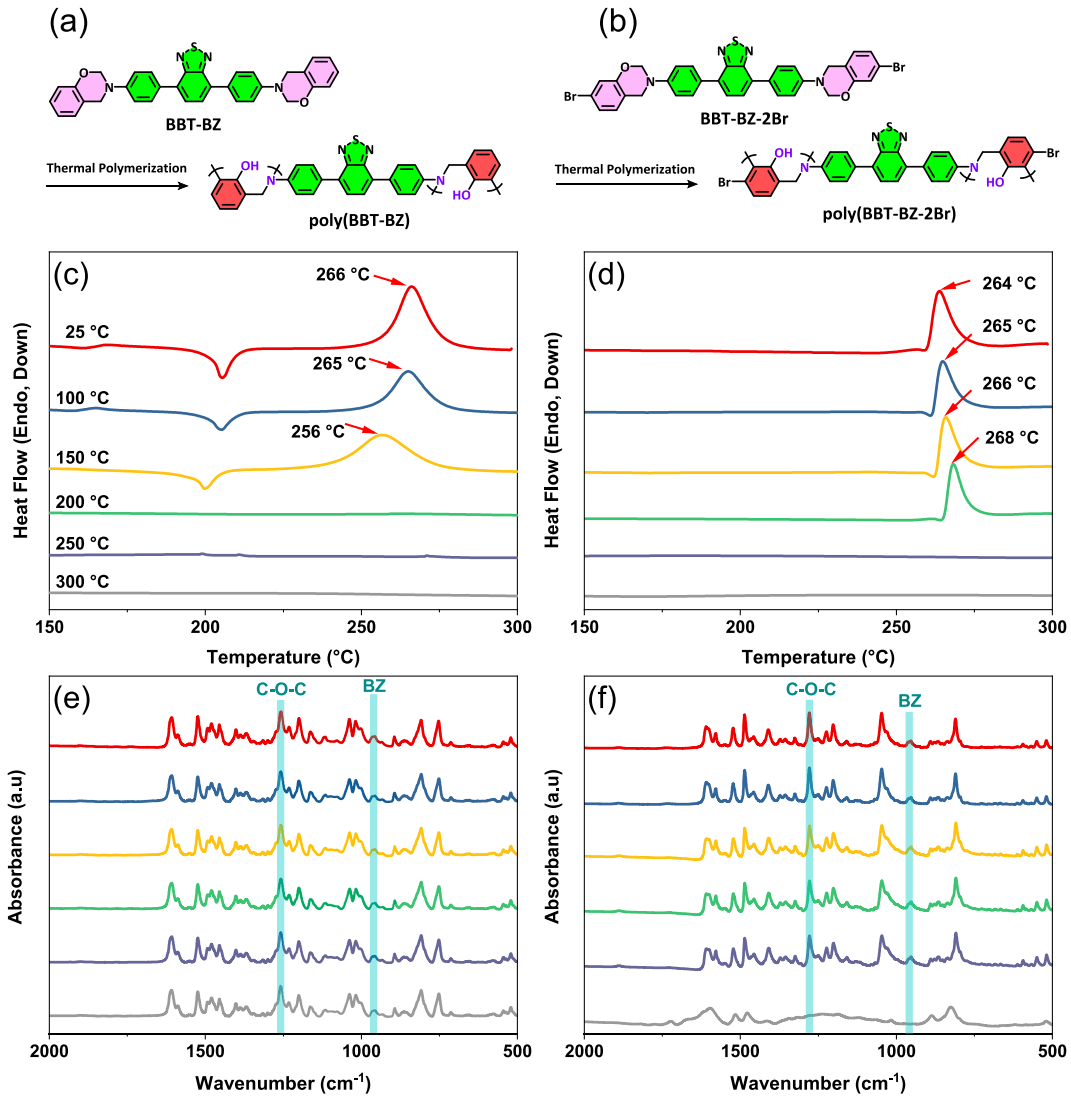

Fig. 3. The preparation of poly(BBT-BZ) and poly(BBT-BZ-2Br) through ROP. (c, d) DSC analyses and (e, f) FTIR spectra of (c, e) BBT-BZ and (d, f) BBT-BZ-2Br at different curing temperatures.

(6.42 ppm), and $NHCH_2$ (4.24 ppm) were observed, as shown in Fig. 2 (c). After the final Mannich condensation to form BBT-BZ-2Br monomer, the characteristic peaks representing aromatic protons (7.90–6.55 ppm), OCH_2N (b, 5.58 ppm), and $ArCH_2N$ (c, 4.73 ppm) appeared, as shown in Fig. 2(c). The signal ratio of OCH_2N and $ArCH_2N$ is 1:1, which is due to the presence of oxazine ring protons. Similarly, after reduction to form BBT-Red-2Br compound, the ^{13}C NMR signals of aromatic carbons (157.35–112.60 ppm) and $HNCH_2$ (a, 40.98 ppm) could be observed. After the final Mannich condensation obtained BBT-BZ-2Br monomer, unit signals representing aromatic carbons (154.05–110.47 ppm), OCH_2N (c, 78.06 ppm), and $ArCH_2N$ (b, 48.10 ppm) could be found in the ^{13}C NMR spectrum. We could confirm that the chemical structure of the BBT-BZ-2Br monomer was synthesized with high purity in this study. HR ES-MS spectrometry [**Figs. S4–S6 and Table S1**] confirmed the molecular weights of BBT-SF-2Br, BBT-Red-2Br, and BBT-BZ-2Br, supporting the successful synthesis of the BBT-BZ-2Br via a three-step route and indicating high structural purity.

3.3. Thermal polymerization behavior of BBT-BZ and BBT-BZ-2Br monomers

Both BBT-BZ and BBT-BZ-2Br monomers undergo the thermal ROP from 25 °C to 300 °C every two hours, which is characterized by using DSC and FTIR analyses to explore their chemical structures and thermal polymerization behavior. Firstly, the BBT-BZ monomer, as shown in Fig. 3(a), is the scheme of its thermal ring-opening polymerization (ROP) behavior. Fig. 3(c) shows its corresponding thermal ROP behavior by using DSC analyses. It was found that the BBT-BZ monomer without thermal treatment has a curing exothermic peak at 266 °C, which is similar to a typical Pa-type monomer (263 °C). As the thermal ROP temperature increases, this exothermic peak gradually decreases, and after thermal ROP at 200 °C for two hours, this curing exothermic peak completely disappears, indicating the completion of thermal ROP. At the same time, in the FTIR spectra, as shown in Fig. 3(e), we focus on the absorption signals of benzoxazine at 1200 (C—O stretching) and 956 (oxazine ring) cm^{-1}. We found that as the thermal ROP temperature increases, these two signals gradually decrease. When it is at 200 °C, it disappears completely, indicating the completion of thermal ROP, which corresponds to the DSC data. In addition, Fig. 3(b) shows the scheme of the thermal ROP characteristics of the BBT-BZ-2Br. In the DSC analyses of Fig. 3(d), the uncured BBT-BZ-2Br monomer has a curing exothermic peak at 264 °C, which is similar to the BBT-BZ monomer since only two bromine units have existed for BBT-BZ-2Br monomer. Similarly, we found that with the rise in thermal ROP temperature, the exothermic peak progressively diminished. After heating at 250 °C for two hours, the curing exothermic peak had completely disappeared, indicating the

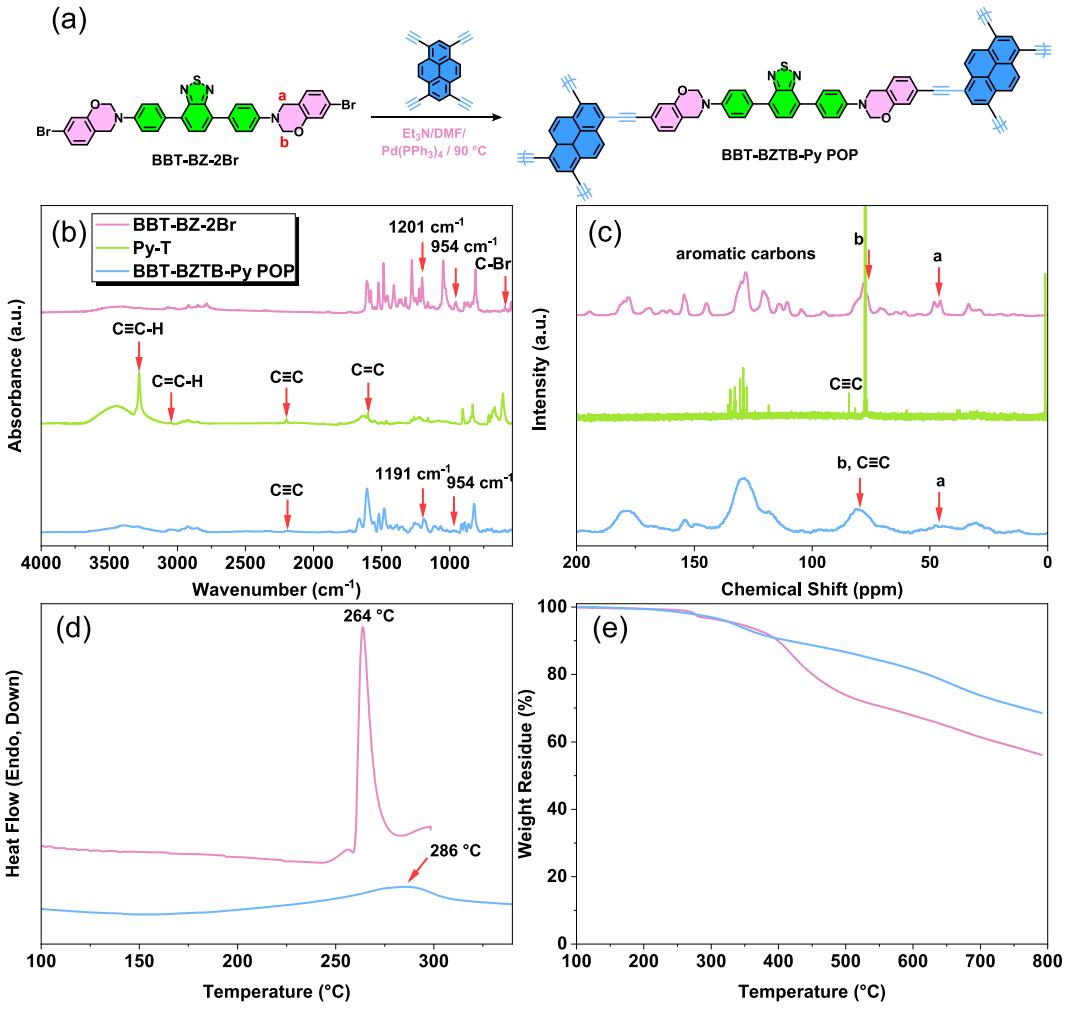

Fig. 4. (a) Synthesis of BBT-BZTB-Py POP, (b) FTIR, and (c) ^{13}C NMR spectra of BBT-BZ-2Br, Py-T, and BBT-BZTB-Py POP. (d) DSC, and (e) TGA analysis of BBT-BZ-2Br and BBT-BZTB-Py POP.

finalization of the thermal ROP process. This result can be further confirmed through FTIR spectra. As shown in Fig. 3(f), the important characteristic signals representing benzoxazine at 1201 and 954 cm^{-1} were gradually decreased as the thermal ROP temperature increased and even disappeared completely at 300 °C. Instead, a broad peak appears, representing the OH group, indicating the thermal ROP occurred.

3.4. Synthesis and thermal ROP behavior of the BBT-BZTB-Py POP

Fig. 4(a) shows the scheme for producing BBT-BZTB-Py POP was constructed using the Sonogashira reaction of Py-T and BBT-BZ-2Br units, and FTIR and solid-state CP/MAS NMR spectroscopy are measured at room temperature to observe the changes in characteristic functional groups. Next, DSC and TGA are also used to observe its thermal behavior. In the FTIR spectra, as shown in Fig. 4(b), we could observe the characteristic peak of Py-T at 3290 cm^{-1} due to the C ≡ C-H unit and C—Br at 593 cm^{-1} of BBT-BZ-2Br, both disappearing for BBT-BZTB-Py POP, and the corresponding C≡C (2191 cm^{-1}), C-O-C (1191 cm^{-1}), and the oxazine ring (954 cm^{-1})remained, confirming that the benzoxazine unit was successfully added to BBT-BZTB-Py POP. In the ^{13}C NMR spectra, as shown in Fig. 4(c), the presence of the characteristic peaks OCH_2N (b, 80.84 ppm) and $ArCH_2N$ (a, 47.65 ppm) of BBT-BZTB-Py POP could also be observed, further confirming the success of the synthesis for BBT-BZTB-Py POP. Furthermore, Fig. 4(d) shows the DSC thermal analyses, and we found that BBT-BZTB-Py POP has a higher and broader curing exothermic peak at 286 °C compared with the BBT-BZ-2Br monomer (286 °C). This is because the cross-linked structure generated by the Sonogashira Hagihara coupling reaction imposes restrictions on the ROP of the oxazine ring, so the exothermic peak increases. Similarly, compared with BBT-BZ-2Br about TGA analyses [Fig. 4(e)], after the Sonogashira reaction, BBT-BZTB-Py POP has a more extensively cross-linked structure, and its thermal properties steadily increase (T_{d10} from 399 °C to 415 °C and char yield from 56.0 wt% to 68.5 wt%). To comprehend the porosity of BBT-BZTB-Py POP, the N_2 adsorption/desorption isotherm was measured at 77 K, as displayed in Fig. 5(a). It could be observed that under low relative pressure ($P/P_0 < 0.1$), the adsorption/desorption curve rises sharply and appears convex upward, showing that the relationship between the material and N_2 has strong van der Waals interactions. Under high relative pressure, the adsorption/desorption isotherm curve does not overlap, and a hysteresis loop appears. Therefore, based on the IUPAC classification, this isotherm corresponds to a type IV curve with the specific surface area (SA_{BET}) of BBT-BZTB-Py POP being 56 $m^2\ g^{-1}$, accompanied by a total pore volume (V_{total}) of 0.36 $cm^3\ g^{-1}$. We determined the average pore size diameter using the NLDFT method, as shown in Fig. 5(b), which ranges from 1.72 to 3.41 nm and 3.96 to 6.02 nm, indicating that the pore size distribution is in micropores and mesopores. In addition, we used TEM and SEM to observe and analyze the morphology of BBT-BZTB-Py POP. Figs. 5(c)-5(d) display TEM images, indicating an irregular and disordered structure. Fig. 5(e) displays SEM images, also showing that the material is composed of many interconnected, irregular, and small spheres. In addition, based on SEM-EDS analysis as shown in Figs. 5**(f-i)**, implying

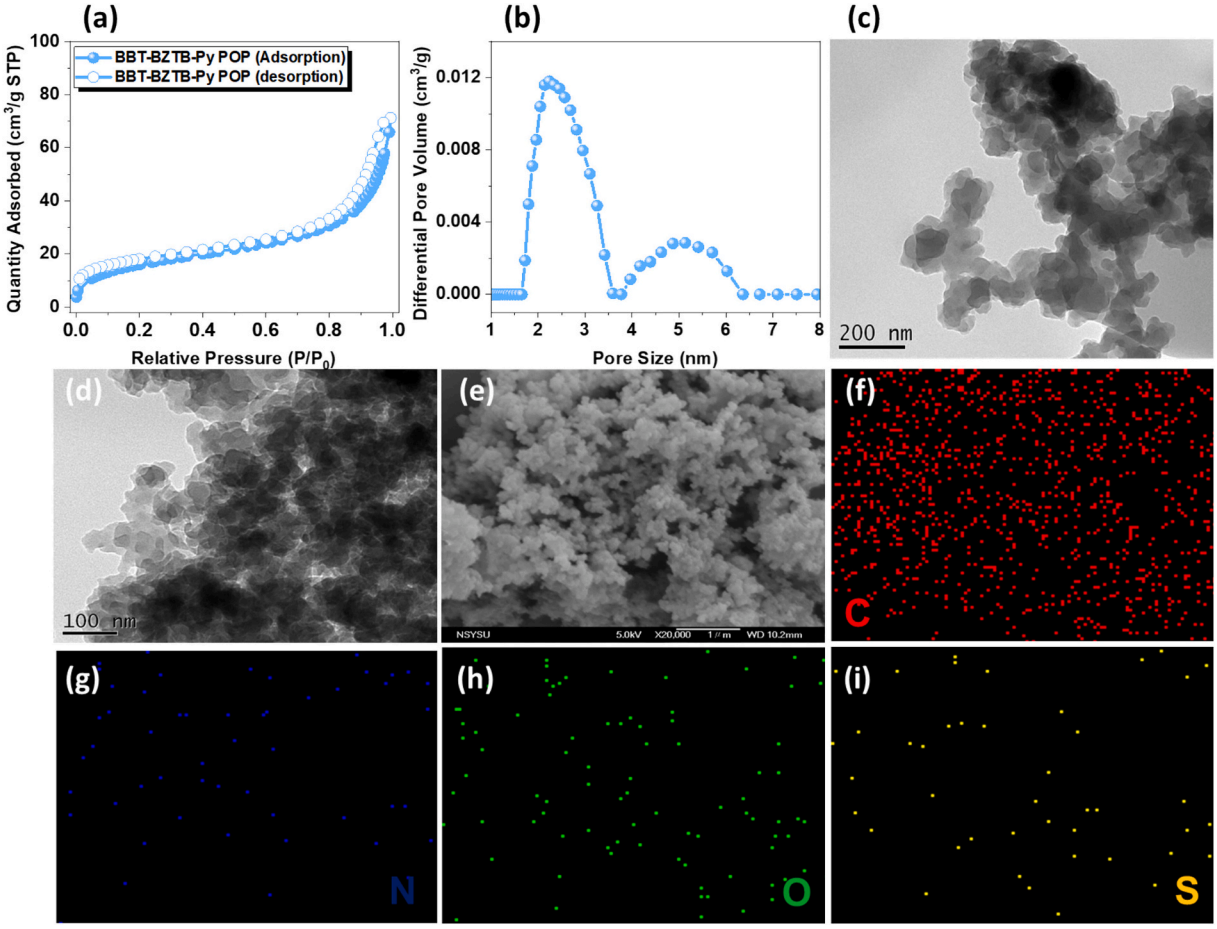

Fig. 5. (a) N_2 adsorption/desorption isotherm curve, (b) pore size distribution, (c, d) TEM image, (e) SEM image, and (f, g, h, i) SEM-EDS images of poly(BBT-BZTB-Py) POP [the scale is 30 μm].

the C, N, O, and S mappings, respectively, and the existence and proportion of C (red), N (blue), O (green) and S(yellow) atoms evenly in BBT-BZTB-Py POP. Next, we thermal-treated BBT-BZTB-Py POP at 300 °C for three hours to form poly(BBT-BZTB-Py) POP, as seen in Fig. 6 (a). Then, we could explore the ROP behavior of BBT-BZTB-Py POP through DSC, solid-state NMR, FTIR, and TGA analyses. DSC results as shown in Fig. 6(b), uncured BBT-BZTB-Py POP at room temperature showed a thermal polymerization exothermic peak at 286 °C. However, when the monomer was heated at 300 °C for 3 h to form poly(BBT-BZTB-Py) POP, the exothermic peak disappeared, indicating complete thermal ROP. In the FTIR spectra [Fig. 6(c)], the signals of BBT-BZTB-Py POP appear at 1191 and 933 cm^{-1} for BZ units. When heated to 300 °C for 3 h, the signals disappear, and broad peaks appear at 3689–3000 cm^{-1}. This broad peak is due to the large number of OH groups generated after the BBT-BZTB-Py POP ring opens to form poly(BBT-BZTB-Py) POP, which could form a large number of intermolecular and intramolecular hydrogen bonding forces, which is beneficial to subsequent experiments. In the solid-state ^{13}C NMR spectrum [Fig. 6(d)], it could be found that the signal of oxazine rings weakens at 80.84 ppm (OCH_2N unit overlaps with C≡C unit) and completely disappears at 47.65 ppm ($ArCH_2N$ unit). As shown in Fig. 6(e), the TGA results indicate that the T_{d10} and char yields of BBT-BZTB-Py POP are 415.8 °C and 68.56 wt%, respectively. After ROP was employed to produce poly(BBT-BZTB-Py) POP, the T_{d10} value rose to 426.8 °C, whereas the char yield declined to 61.31 wt%. It is speculated that it may be because the thermal stability of the CH_2 group after thermal ROP is weak and easy to crack at high temperatures. **Table S2** presents the elemental composition of the poly(BBT-BZTB-Py) POP, showing atomic contents of 84.72 % (C), 6.44 % (N), 4.79 % (O), and 4.05 % (S). The high-resolution XPS spectra provide detailed insight into the chemical environments of the elements within the poly(BBT-BZTB-Py) POP. In the C 1 s spectrum [**Figure S7(a)**], three distinct peaks are observed at 284.3, 285.4, and 287.2 eV, corresponding to C–C/C=C, C—N, and C–OH functionalities. The N 1 s spectrum [**Figure S7(b)**] reveals two deconvoluted peaks attributed to C–N–C (398.8 eV) and C=N–S (400.1 eV) moieties. Deconvolution of the O 1 s spectrum [**Figure S7(c)**] confirms the presence of C–OH groups at 532.3 eV. The S 2p spectrum [**Figure S7(d)**] exhibits peaks at 163.6 eV and 165.1 eV, assigned to S—N ($2P_{3/2}$) and S—N ($2P_{1/2}$), respectively. A comprehensive summary of the XPS fitting parameters for C, N, O, and S is provided in **Table S3**. After thermal ROP, TEM and SEM were utilized to investigate and assess the morphology of poly(BBT-BZTB-Py) POP. A disordered structure is observed in the TEM image [**Figure S8(a)**]. In the SEM image [**Figure S8(b)**], it is observed that there are many small and irregular particles on the surface. Additionally, in the EDS analysis of SEM [**Figs. S8(c-f)**], the distribution pattern of C, N, O, and S elements of poly(BBT-BZTB-Py) POP was evenly distributed and was confirmed by mapping the sample.

3.5. Characterization of the poly(BBT-BZTB-Py) POP-600

In order to prepare N/S co-doped microporous carbon materials, as shown in Fig. 7(a), we carbonized the poly(BBT-BZTB-Py) POP at 600 °C and used the KOH activation method to synthesize poly(BBT-BZTB-Py) POP-600 and used Raman spectroscopy, XRD, and XPS to identify and explore its microstructure. In the Raman profile, as presented in Fig. 7 (b), there are two signals at 1337 and 1593 cm^{-1}, representing the D

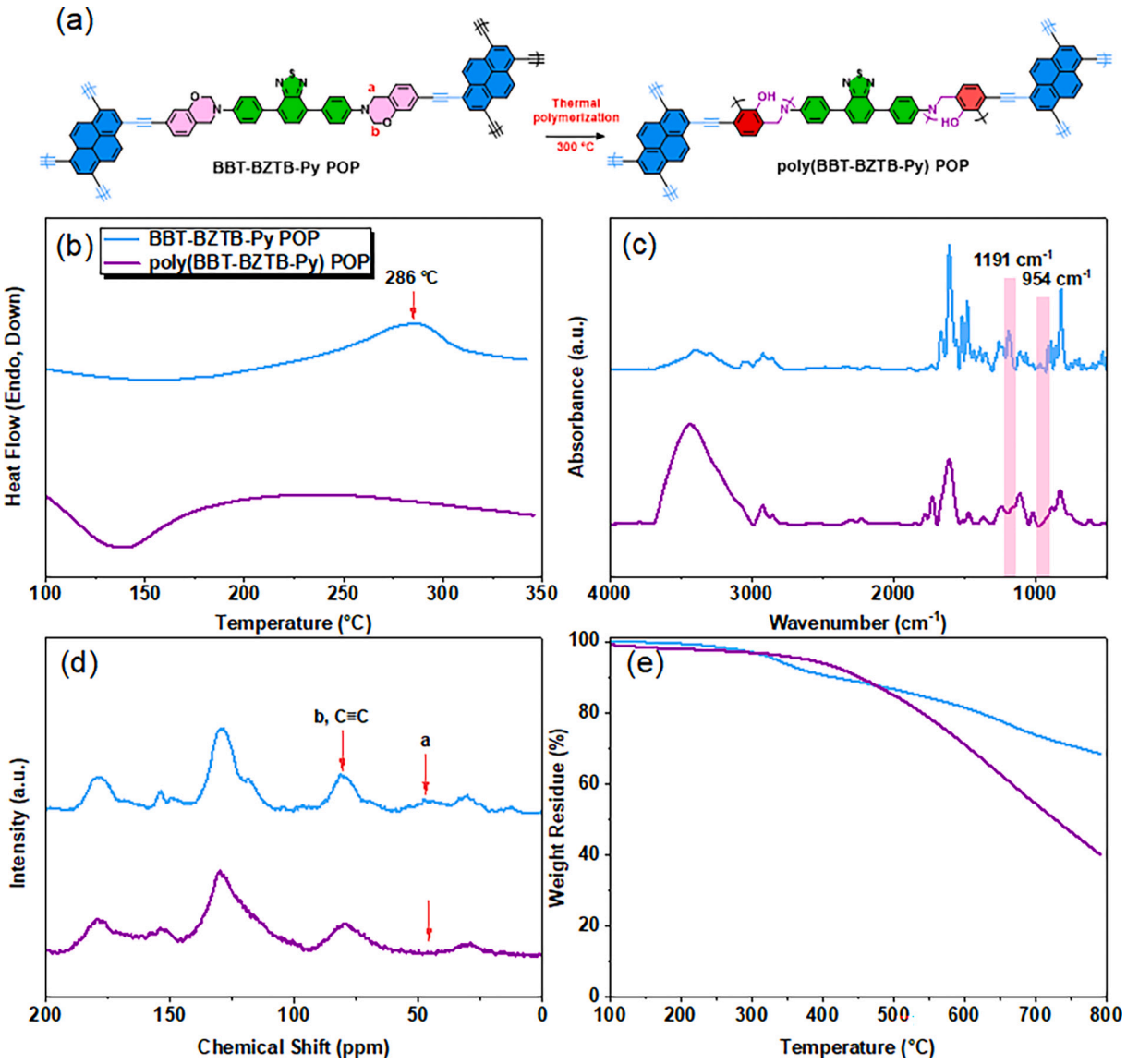

Fig. 6. (a) Synthesis of poly(BBT-BZTB-Py) POP through ROP, (b) DSC analyses, (c) FTIR and (d) solid-state ^{13}C NMR spectra, and (e) TGA traces of BBT-BZTB-Py POP and poly(BBT-BZTB-Py) POP.

band and G band, respectively, which are the main characteristic peaks of graphitic carbon materials. The D band, also known as the disorder band, represents the defects and disorder of the carbon material structure, and its defects are proportional to the intensity, while the G band represents the vibration mode of graphene sp^2 hybridized carbon atoms. In addition, the degree of graphitization of the material could be evaluated based on the ratio of intensities between the D band and the G band. From the data, the I_D/I_G value of poly(BBT-BZTB-Py) POP-600 is 0.87. Next, the graphite structure after the carbonization of the material was studied through XRD analysis. In Fig. 7(c), we focus on the wide diffraction peaks centered at 25° and 44°, which are associated with the plane of (002) and (100) for the hexagonal graphite lattice, respectively. Like other heteroatom co-doped graphene published in the past, these two broad diffraction peaks appeared [55–58]. In the XPS survey spectrum, as shown in Fig. 7(d), we could observe four signals corresponding to C1s, N1s, O1s, and S2p, respectively, confirming the successful introduction of N and S atoms into poly(BBT-BZTB-Py) POP-600, and then perform peak fitting on the signals of these four orbits, respectively.

As detailed in **Table S2**, the elemental composition of the poly(BBT-BZTB-Py) POP-600 comprises 67.64 % carbon, 5.13 % nitrogen, 26.62 % oxygen, and 0.6 % sulfur by atomic percentage. First, in the C1s spectra [Fig. 7(e)], In the C1s spectra, four peaks are observed at 284.5, 285.9, 287.5, and 287.8 eV, corresponding to C-C/C=C, C—N, C=O, and C-O/C-S groups, respectively [56]. Similarly, the N1s spectra [Fig. 7(f)] reveal four deconvoluted peaks: pyridinic nitrogen (N-6, 397.97 eV), pyrrolic nitrogen (N-5, 399.27 eV), quaternary nitrogen (N-Q, 400.77 eV), and pyridine-N-oxide (N-X, 403.57 eV). In terms of gas capture, N-5 and N-6 have strong interactions with CO_2 molecules, which facilitate CO_2 capture. In terms of electrochemistry, since N-5 and N-6 have excellent electron donor properties and high charge transfer capabilities [59,60], the introduction of carbon materials could enhance the capacitance value and could even cause redox reactions with alkaline electrolytes to help with pseudocapacitance. Furthermore, N-Q could promote charge transfer between the electrode and the electrolyte [61,62]. Fig. 7(g) presents the deconvolution results of the O1s spectra, highlighting the presence of functional groups such as C=O (530.9 eV), C-OH (532.3 eV), and C-O-C (533.6 eV) [56]. Fig. 7(h) displays the fitting analyses of the S2p spectra, showing that peaks representing thiophene-S (C—S $2P_{1/2}$, C—S $2P_{3/2}$) and sulfone (O=S=O) were found at 162.1, 164.2, and 168.3 eV [56,62], where S atoms have higher electrochemical activity, and doping them into carbon materials could bring more active sites and cause electrochemical reversible reactions

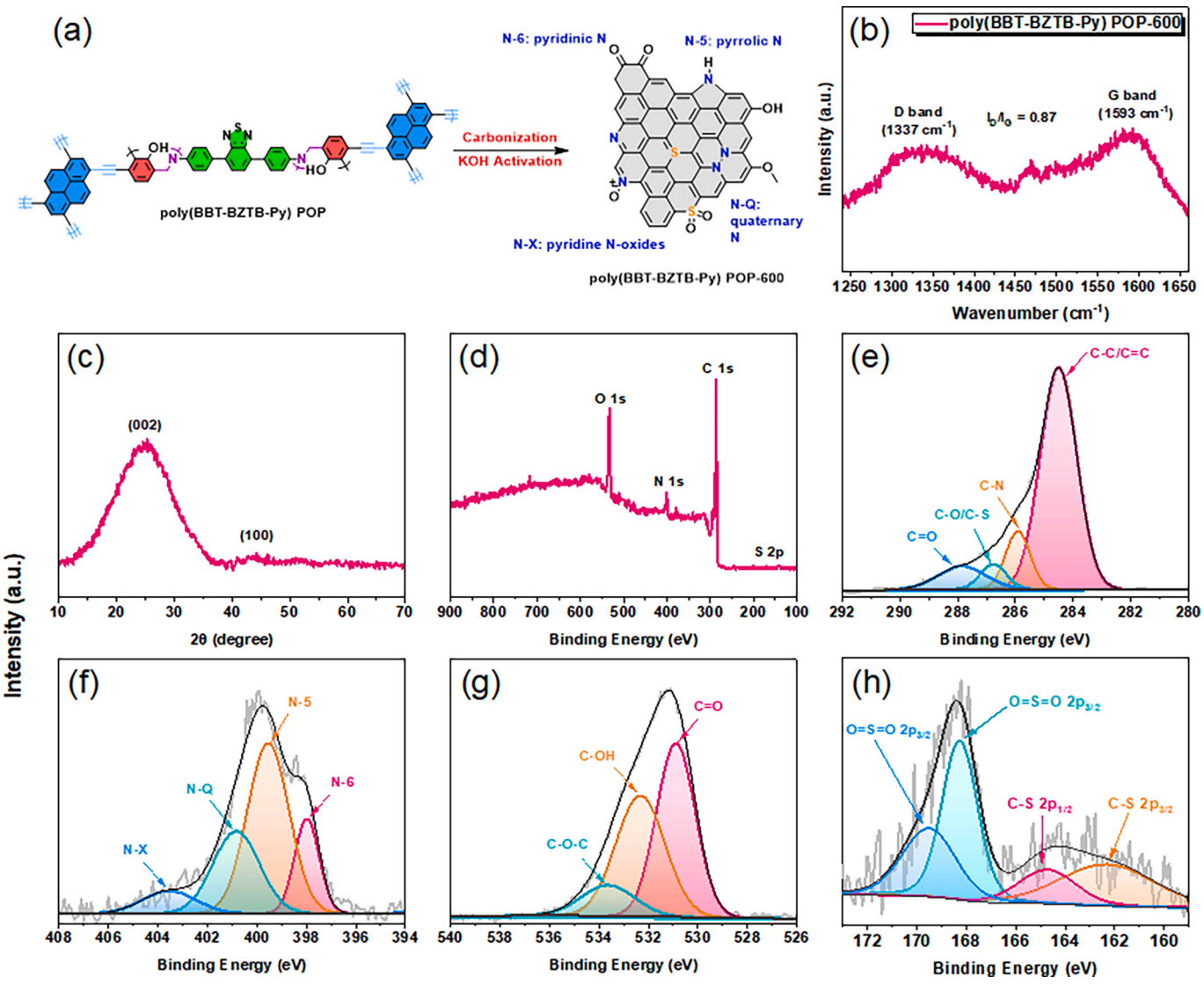

Fig. 7. (a) Preparation of poly(BBT-BZTB-Py) POP-600 using poly(BBT-BZTB-Py) POP precursor. (b) Raman spectrum, (c) XRD pattern, (d) XPS survey spectrum of poly(BBT-BZTB-Py) POP-600. (e-h) Deconvolution spectra of (e) C1s, (f) N1s, (g) O1s, and (h) S2p scan profiles recorded for the poly(BBT-BZTB-Py) POP-600.

[62]. All XPS fitting results for each C, N, O, and S are summarized in **Table S3**. Fig. 8(a) displays the N_2 isotherm curve of poly(BBT-BZTB-Py) POP-600, which belongs to Type I and Type IV like most porous carbons prepared by the KOH activation method, and there is a H4 hysteresis loop in the second half of the isotherm curve, indicating the presence of some mesopores the SA_{BET} of poly(BBT-BZTB-Py) POP-600 increased to 726 $m^2\ g^{-1}$ and the V_{total} was 0.52 $cm^3\ g^{-1}$ and average pore diameters of 0.43–1.79 nm [Fig. 8(b)] through the NLDFT method, proving that poly(BBT-BZTB-Py) POP-600 is a microporous carbon material. We also used TEM and SEM to observe the morphological characteristics of N/S co-doped microporous carbon materials. From the TEM images [Figs. 8 (c) and 8(d)], it could be seen that poly(BBT-BZ-Py) POP-600 also has a disordered structure and belongs to amorphous carbon. The SEM image [Fig. 8(e)] shows a structure similar to layered graphite. Furthermore, in the EDS analyses of SEM, Figs. 8**(f-i)** display the elemental mappings of C, N, O, and S, confirming both the presence and uniform distribution of these elements in poly(BBT-BZTB-Py) POP-600.

3.6. CO_2 capture analyses

We conducted CO_2 capture experiments with BBT-BZTB-Py POP, poly(BBT-BZTB-Py) POP, and poly(BBT-BZTB-Py) POP-600 at 298 K and 273 K, respectively, under 1 bar. Fig. 9(a) shows that at 298 K, the capture amounts were 0.99 mmol g^{-1} (4.36 wt%), 1.49 mmol g^{-1} (6.56 wt%), and 4.46 mmol g^{-1} (19.62 wt%), respectively. Fig. 9(b) shows that at 273 K, the capture amounts were 1.29 mmol g^{-1} (5.68 wt%), 2.25 mmol g^{-1} (9.90 wt%), and 5.58 mmol g^{-1} (24.55 wt%), respectively. The results confirmed that after the formation of poly(BBT-BZTB-Py) POP via thermal ROP, an abundant amount of O and N active adsorption sites appeared due to solid-state chemical conversion. It could generate strong intermolecular hydrogen bonds of CO_2 molecules with [OH···O═C] and [N···O═C], so the capture ability increases. When poly(BBT-BZTB-Py) POP-600 is formed by carbonization and KOH activation, the key to having a high capture capacity (5.58 mmol g^{-1}) at 1 bar and 273 K is because of the high SA_{BET} (726 $m^2\ g^{-1}$), micropores (0.43–1.79 nm), and pyrrolic nitrogen (N-5), all of which are beneficial to CO_2 capture. **Figure S9** displays the standard deviation profiles of CO_2 uptake at 298 K following three consecutive adsorption cycles for poly(BBT-BZTB-Py) POP and poly(BBT-BZTB-Py) POP-600. Furthermore, based on the Clausius-Clapeyronequation, the isosteric adsorption heats (Q_{st}) of the material could be obtained. At a capture capacity of approximately 0.99 mmol g^{-1}, the Q_{st} of BBT-BZTB-Py POP, poly(BBT-BZTB-Py) POP, and poly(BBT-BZTB-Py) POP-600 were 9.09, 27.78, and 35.59 KJ mol^{-1}, respectively. We found that poly(BBT-BZTB-Py) POP-

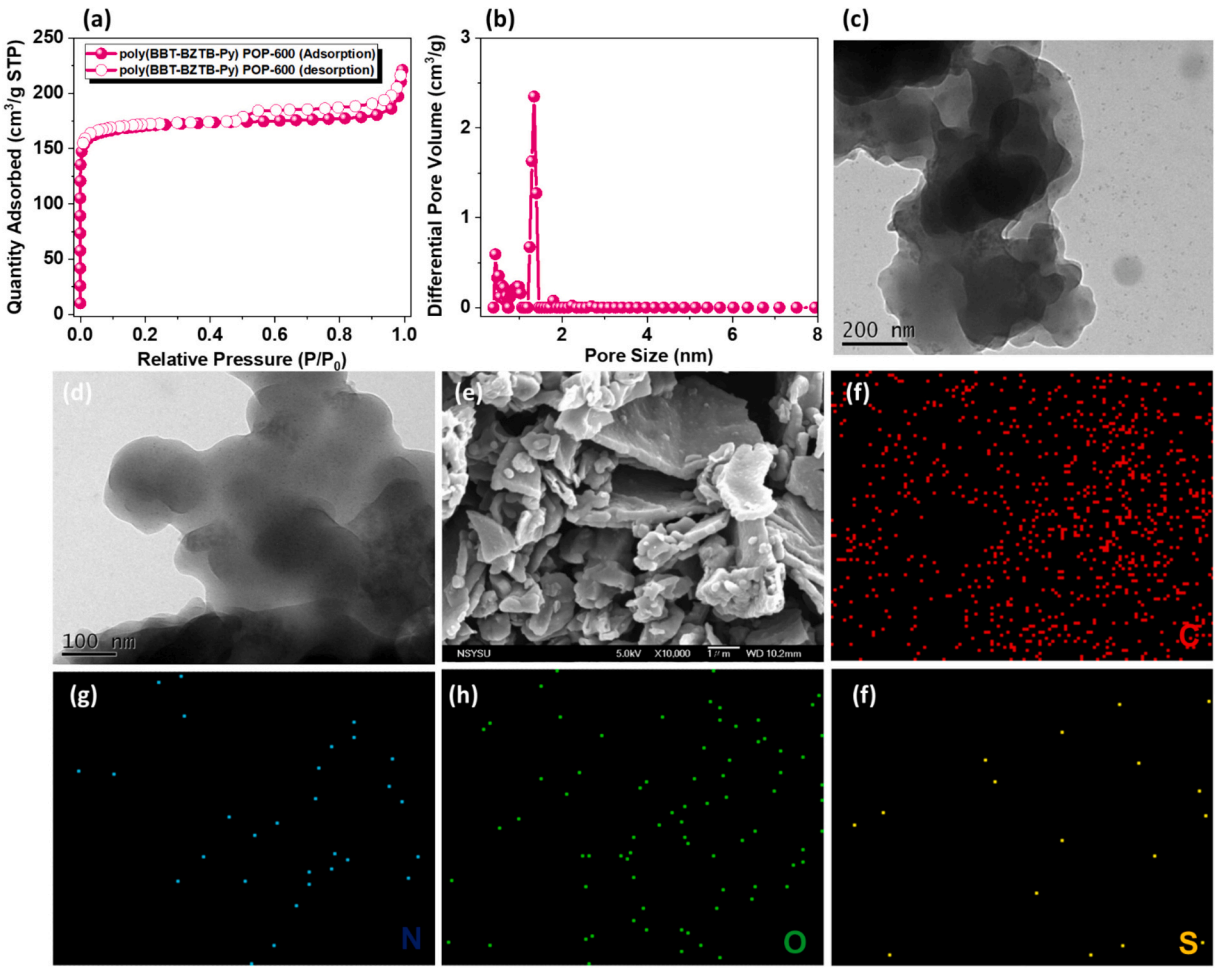

Fig. 8. (a) N_2 adsorption/desorption isotherm curve, (b) pore size distribution, (c, d) TEM image, (e) SEM image, and (f, g, h, i) SEM-EDS images of poly(BBT-BZTB-Py) POP-600 [the scale is 30 μm].

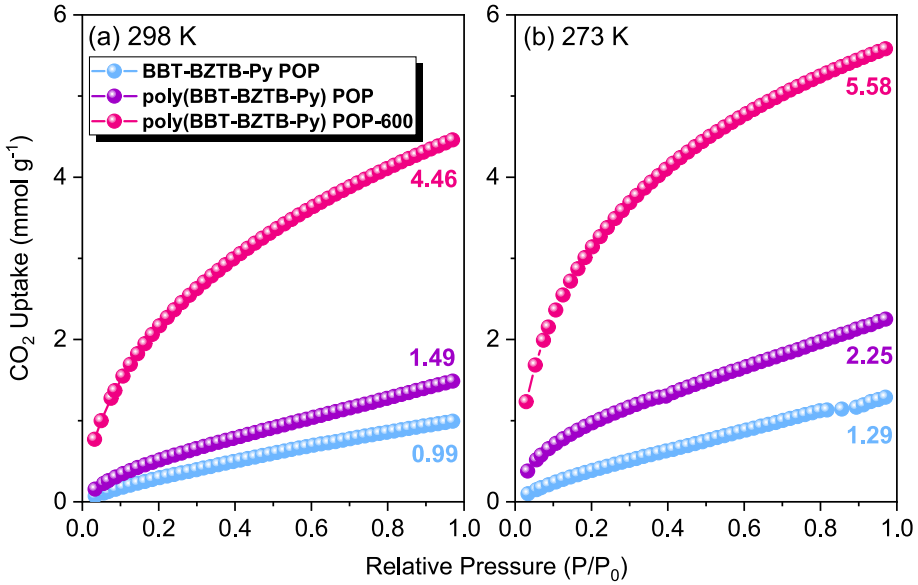

Fig. 9. CO_2 adsorption capacities of BBT-BZTB-Py POP, poly(BBT-BZTB-Py) POP, and poly(BBT-BZTB-Py) POP-600 at (a) 298 K and (b) 273 K, under 1 bar.

600 has a greater heat of adsorption than the other two materials, further confirming that compared to BBT-BZTB-Py POP and poly(BBT-BZTB-Py) POP, poly(BBT-BZTB-Py) POP-600 has a stronger interaction with CO_2, which is also the reason for the high CO_2 capture capacity. **Table S5** presents a compilation of recently reported microporous carbon materials for CO_2 capture, including AT-F2–600, BZPh-A,

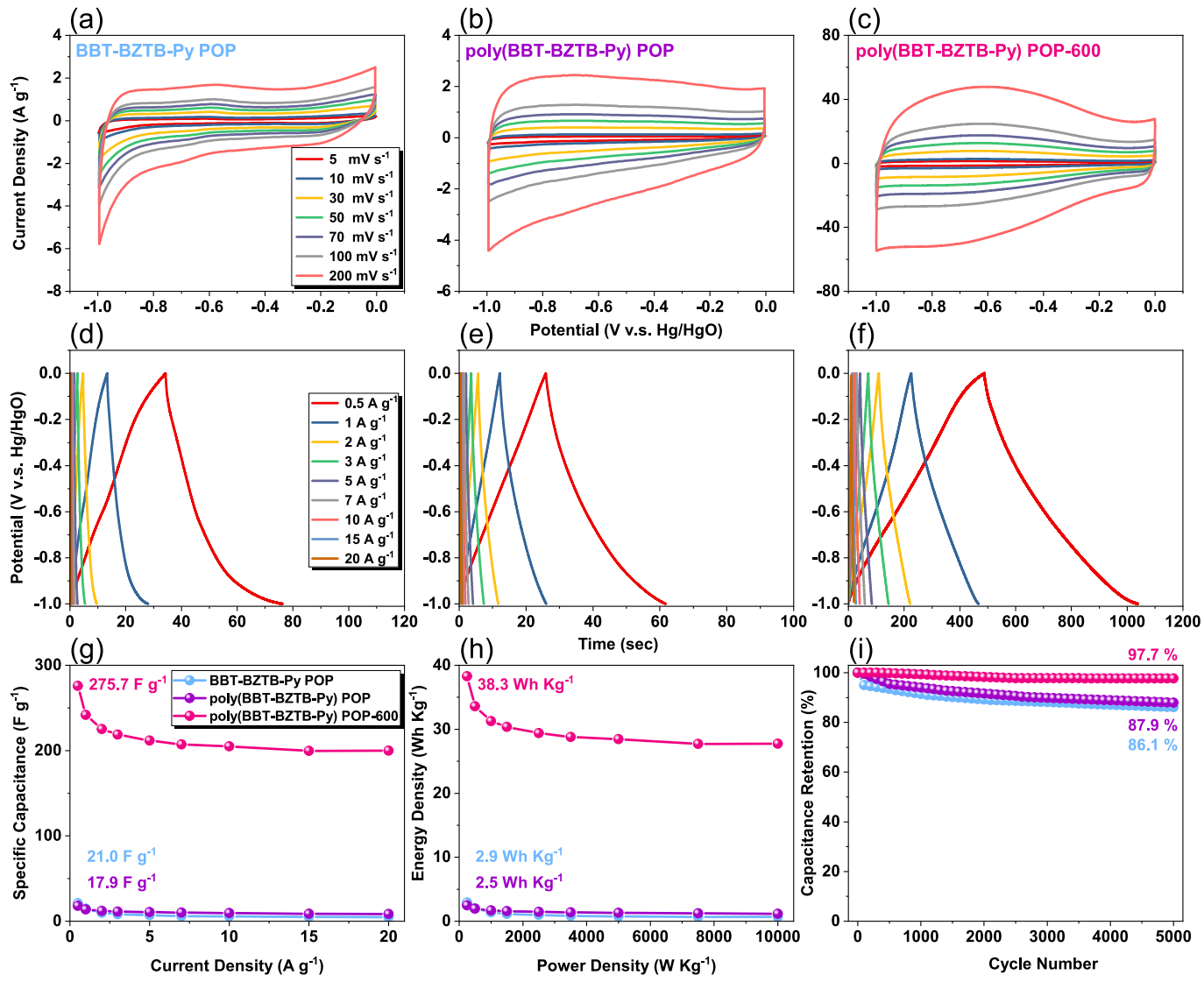

Fig. 10. (a, b, c) CV and (d, e, f) GCD curves of (a, d) BBT-BZTB-Py POP, (b, e) poly(BBT-BZTB-Py) POP, and (c, f) poly(BBT-BZTB-Py) POP-600. (g) Specific capacitance, (h) Ragone plot, and (i) capacitance retention of BBT-BZTB-Py POP, poly(BBT-BZTB-Py)POP and poly(BBT-BZTB-Py)POP-600.

N0.8A80F50, and TPE-CPOP1–800. The poly(BBT-BZTB-Py) POP-600 synthesized in this study exhibits superior CO_2 capture capacities at both 298 K and 273 K compared to these materials. BZs have emerged as a promising nitrogen-rich precursor for the fabrication of microporous carbon materials. Its unique nitrogen-containing functional groups, combined with its microporous structure, offer significant potential to enhance CO_2 adsorption capacity, making it a viable candidate for CO_2 capture applications.

3.7. Electrochemical analyses

The electrochemical behavior of BBT-BZTB-Py POP, poly(BBT-BZTB-Py) POP, and poly(BBT-BZTB-Py) POP-600 in a three-electrode system is evaluated by cyclic voltammetry (CV) and galvanostatic charge/discharge (GCD) curves in 6 M KOH and potential window (from −1 to 0 V), as shown in Fig. 10. The CV curves of all samples present a rectangular-like shape at 200 mV s^{-1}, and all have wider hump peaks, as shown in Figs. 10**(a-c)**, demonstrating the primary storage mechanism is electric double-layer capacitance (EDLC), with pseudocapacitance contributing only a minor portion [63–65]. In addition, compared with BBT-BZTB-Py POP and poly(BBT-BZTB-Py) POP, poly(BBT-BZTB-Py) POP-600 exhibits a larger curve area because of its high SA_{BET} (726 $m^2\ g^{-1}$) and higher active N species content. In the GCD curve [Figs. 10 **(d-f)**], with no noticeable voltage drop, the three samples exhibited a highly symmetrical triangular shape at 0.5 A g^{-1}, indicating efficient ion transfer and reversible ionic adsorption-desorption processes [66,67]. This highlights excellent conductivity and minimal resistance. At 0.5 A g^{-1}, BBT-BZTB-Py POP, poly(BBT-BZTB-Py) POP, and poly(BBT-BZTB-Py) POP-600 exhibit specific capacitances of 21.0, 17.9, and 275.7 F g^{-1}, respectively [Fig. 10**(g)**]. Compared with the first two samples, the GCD curve of poly(BBT-BZTB-Py) POP-600 is symmetrical and closer to an isosceles triangle. As shown in Fig. 10**(g)**. At 10 Ag^{-1}, the specific capacitance of poly(BBT-BZTB-Py) POP-600 is still as high as 205 F g^{-1}; at 20 A g^{-1}, it is still 200 F g^{-1}. The results presented in **Table S6** highlight the strong performance of our poly(BBT-BZTB-Py) POP-600 compared to several carbon-based polymers. Fig. 10**(h)** displays the Ragone plot, indicating that poly(BBT-BZTB-Py) POP-600 has a higher energy density (38.3 Wh kg^{-1}) than BBT-BZTB-Py POP (2.9 Wh kg^{-1}) and poly(BBT-BZTB-Py) POP (2.5 Wh kg^{-1}). The capacitance retention rates of BBT-BZTB-Py POP, poly(BBT-BZ-Py) POP, and poly(BBT-BZTB-Py) POP-600 after 5000 charge-discharge cycle tests at 10 A g^{-1} [Fig. 10 **(i)**] are 86.1 %, 87.9 %, and 97.7 %, respectively, all with good cycling stability.

Supercapacitor charge storage involves surface and diffusion-

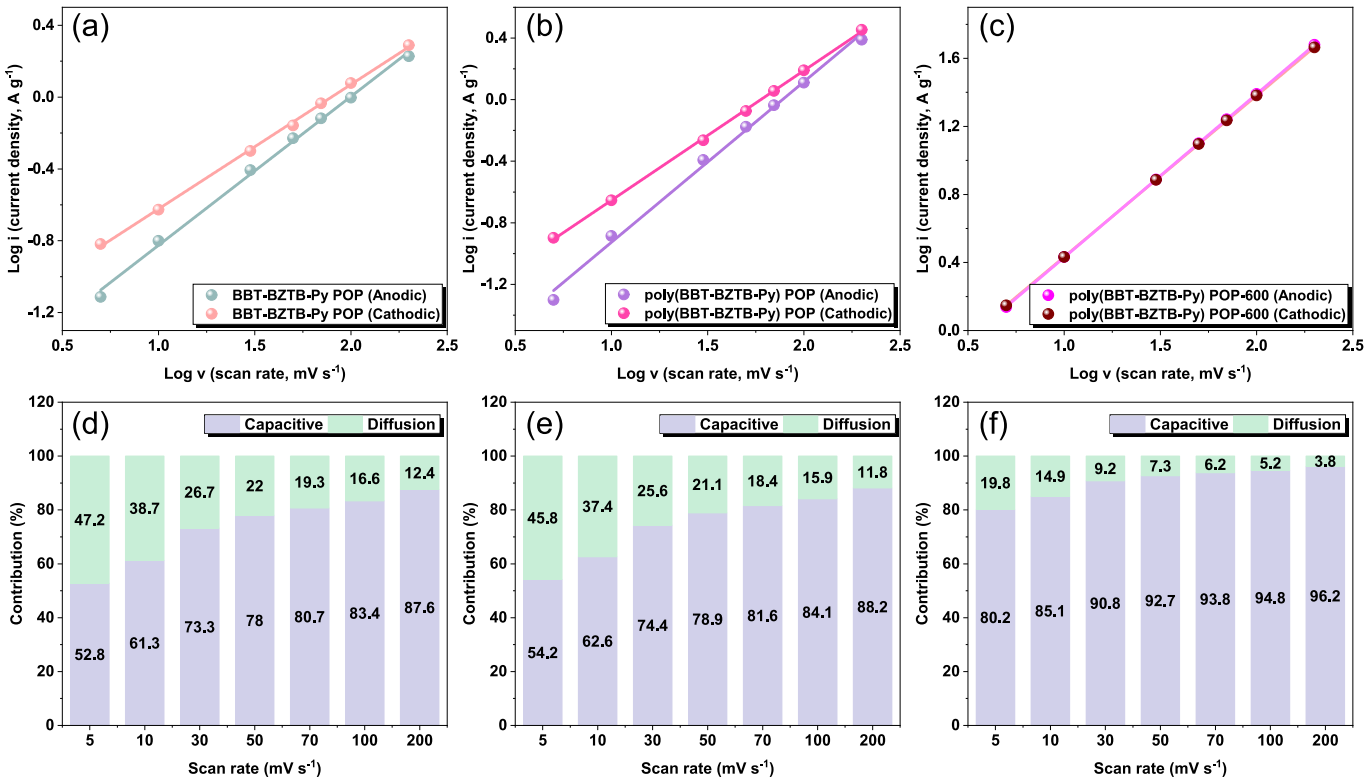

Fig. 11. Plots of log(i) versus log(v) for (a) BBT-BZTB-Py POP, (b) poly(BBT-BZTB-Py) POP, and (c) poly(BBT-BZTB-Py) POP-600.The relative contributions of capacitance and diffusion to charge storage for (d) BBT-BZTB-Py POP, (e) poly(BBT-BZTB-Py) POP, and (f) poly(BBT-BZTB-Py) POP-600 at different scan rates.

controlled capacitance. The b value is derived from the slope of the log (I) vs. log(v) plot, following the power-law relationship between current and scan rate, as shown in Figs. 11**(a-c)**. The estimated b values for BBT-BZTB-Py POP are 0.83 and 0.69; for poly(BBT-BZTB-Py) POP, they are 0.92 and 0.84; and for poly(BBT-BZTB-Py) POP-600, they are 0.96 and 0.95. When b = 0.5, the charge storage mechanism belongs to diffusion control capacitance, and when b = 1, it belongs to surface capacitance [68–70]. Therefore, through the b value, it is confirmed that BBT-BZTB-Py POP, poly(BBT-BZTB-Py) POP, and poly(BBT-BZTB-Py) POP-600 belong to the coexistence of EDLC and PC in terms of energy storage mechanisms but are more inclined to EDLC. Next, the capacitance contribution is quantified through Dunn's formula, as shown in Figs. 11 (d-f). At a scan rate of 5 mV s^{-1}, the surface capacitance contribution values of BBT-BZTB-Py POP, poly(BBT-BZTB-Py) POP, and poly(BBT-BZTB-Py) POP-600 are 52.8 %, 54.2 %, and 80.2 %, respectively. As the scan rate increases, the contribution of diffusion control decreases because ions do not have time to diffuse at high scan rates. However, in comparison, poly(BBT-BZTB-Py) POP-600 has the highest surface capacitance contribution and the highest specific capacitance.

4. Conclusions

In this study, we have successfully synthesized two benzoxazine monomers, BBT-BZ and its brominated derivative of BBT-BZ-2Br, using a streamlined three-step process. These monomers were thoroughly characterized, and their thermal ROP behavior demonstrated the formation of highly stable cross-linked polymer networks. Additionally, the incorporation of bromine allowed for further functionalization, leading to the synthesis of BBT-BZTB-Py POP via the Sonogashira-Hagihara coupling reaction. The subsequent carbonization and activation of poly(BBT-BZTB-Py) POP produced a nitrogen/sulfur co-doped microporous carbon material, poly(BBT-BZTB-Py) POP-600, featuring a hierarchical microporous and mesoporous structure. This microporous carbon material exhibited excellent properties suitable for gas capture and energy storage, as confirmed by comprehensive physicochemical analyses. This work highlights the versatility of benzoxazine and POP chemistry for designing functional materials and underscores the potential of these materials for cutting-edge applications in sustainability and energy technology.

CRediT authorship contribution statement

Mohamed Gamal Mohamed: Writing – review & editing, Writing – original draft, Supervision, Methodology, Investigation, Formal analysis, Data curation, Conceptualization. **Chia-Chi Chen:** Formal analysis, Data curation, Conceptualization. **Shiao-Wei Kuo:** Supervision, Resources, Project administration.

Declaration of competing interest

The authors declare that they have no known competing financial interests or personal relationships that could have appeared to influence the work reported in this paper.

Acknowledgements

This study was supported financially by the National Science and Technology Council, Taiwan, under contracts NSTC 113-2223-E-110-001- and 113-2221-E-110-012-MY3. The authors thank the staff at National Sun Yat-sen University for their assistance with the TEM (ID: EM022600) experiments.

Appendix A. Supplementary data

Supplementary data to this article can be found online at https://doi.org/10.1016/j.reactfunctpolym.2025.106286.

Data availability

Data is contained within the article or Supplementary Material.

References

[1] S. Manabe, Role of greenhouse gases in climate change, Tellus A 71 (2022) 1620078.
[2] S.J. Kulkarni, Green house gases – a brief review, Int. J. Res. Rev. 4 (2017) 18–21.
[3] V.A. Edlabadkar, R.U. Soni, A.B.M.S. Ud Doulah, S.Y. Owusu, S. Hackett, J. M. Bartels, N. Leventis, C.S. Leventis, CO_2 uptake by microporous carbon aerogels derived from Polybenzoxazine and analogous all-nitrogen Polybenzodiazine aerogels, Chem. Mater. 36 (2024) 1172–1187.
[4] K.S.K. Reddy, A.M. Varghese, A.E. Ogungbenro, G.N. Karanikolos, Aminosilane-modified ordered hierarchical nanostructured silica for highly-selective carbon dioxide capture at low pressure, ACS Appl. Eng. Mater. 1 (2023) 720–733.
[5] M. Robertson, A.G. Obando, B. Nunez, H. Chen, Z. Qiang, Upcycling mask waste to carbon capture sorbents: A combined experimental and computational study, ACS Appl. Eng. Mater. 1 (2023) 165–174.
[6] E. Sivasurya, R. Atchudan, M.G. Mohamed, A. Thangamani, S. Rajendran, A. Jalil, P.K. Kalambate, D. Manoj, S.W. Kuo, Electrocatalytic conversion of CO_2 into selective carbonaceous fuels using metal-organic frameworks: an overview of recent progress and perspectives, Mater. Today. Chem. 44 (2025) 102538.
[7] A.A. Alhwaige, H. Ishida, S.A. Qutubuddin, Nitrogen-enriched carbon aerogels derived from Polybenzoxazine cross-linked graphene oxide-chitosan hybrid matrix with superior CO_2 capture performance, ACS Appl. Eng. Mater. 2 (2024) 1672–1686.
[8] M.G. Mohamed, A. Basit, C.Y. Shih, S.U. Sharma, T. Mondal, S.W. Kuo, Pyrene-linked covalent organic polymer/single-walled carbon nanotubes hybrids as high-performance electrodes for Supercapacitive energy storage, ACS Appl. Energy Mater. 8 (2025) 3764–3778.
[9] J.M. Cui, Z.X. Zhang, H.Y. Quan, Y. Hu, S.J. Wang, D.Z. Chen, Effect of various ammonium salts as activating additive on the capacitance performance of hierarchical porous carbon derived from camellia husk, J. Energy Storage 51 (2022) 104347.
[10] G.Y. Zhao, C. Chen, D.F. Yu, L. Sun, C.H. Yang, H. Zhang, Y. Sun, F. Besenbacher, M. Yu, One-step production of O-N-S co-doped three-dimensional hierarchical porous carbons for high-performance supercapacitors, Nano Energy 47 (2018) 547–555.
[11] S. Zhang, L.N. Sui, H.Q. Kang, H.Z. Dong, L.F. Dong, L.Y. Yu, High performance of N-doped graphene with bubble-like textures for supercapacitors, Small 14 (2018) 1702570.
[12] J.H. Zhu, J. Yang, R.R. Miao, Z.Q. Yao, X.D. Zhuang, X.L. Feng, Nitrogen-enriched, ordered mesoporous carbons for potential electrochemical energy storage, J. Mater. Chem. A 4 (2016) 2286–2292.
[13] M.G. Mohamed, S.W. Kuo, Crown ether-functionalized Polybenzoxazine for metal ion adsorption, Macromolecules 53 (2020) 2420–2429.
[14] M.G. Mohamed, S.W. Kuo, Functional silica and carbon nanocomposites based on Polybenzoxazines, Macromol. Chem. Phys. 220 (2019) 1800306.
[15] M.G. Mohamed, C.J. Li, M.A.R. Khan, C.C. Liaw, K. Zhang, S.W. Kuo, Formaldehyde-free synthesis of fully bio-based multifunctional Bisbenzoxazine resins from natural renewable starting materials, Macromolecules 55 (2022) 3106–3115.
[16] M. Ejaz, M.G. Mohamed, W.C. Huang, Y.C. Kao, W.C. Chen, S.W. Kuo, Highly thermally stable polyhedral oligomeric silsesquioxane based on diacetal-functionalized polybenzoxazine nanocomposites, Eur. Polym. J. 223 (2025) 113649.
[17] R. Yang, N. Li, C.J. Evans, S. Yang, K. Zhang, Phosphaphenanthrene-functionalized Benzoxazines bearing Intramolecularly hydrogen-bonded phenolic hydroxyl: synthesis, structural characterization, polymerization mechanism, and property investigation, Macromolecules 56 (2023) 1311–1323.
[18] M. Ejaz, M.G. Mohamed, S.W. Kuo, Fluorescent Benzoxazine–Perylene Linked Covalent Organic Polymer as a Sensing Probe for Lead Ions and 2,4,6-Trinitrophenol, ACS Appl. Polym. Mater. 6 (2024) 9170–9179.
[19] S. Mukherjee, N. Amarnath, B. Lochab, Oxazine ring-substituted 4th Generation Benzoxazine Monomers & Polymers: Stereoelectronic effect of phenyl substituents on thermal properties, Macromolecules 54 (2021) 10001–10016.
[20] M.M. Samy, M.G. Mohamed, S.W. Kuo, Pyrene-functionalized tetraphenylethylene polybenzoxazine for dispersing single-walled carbon nanotubes and energy storage, Compos. Sci. Technol. 199 (2020) 108360.
[21] C.Y. Chen, W.C. Chen, M.G. Mohamed, Z.Y. Chen, S.W. Kuo, Highly Thermally Stable, Reversible, and Flexible Main Chain Type Benzoxazine Hybrid Incorporating Both Polydimethylsiloxane and Double-Decker Shaped Polyhedral Silsesquioxane Units through Diels–Alder Reaction, Macromol. Rapid Commun. 44 (2023) 2200910.
[22] K. Zhang, Y. Liu, H. Ishida, Polymerization of an AB-Type Benzoxazine Monomer toward Different Polybenzoxazine Networks: When Diels–Alder Reaction Meets Benzoxazine Chemistry in a Single-Component Resin, Macromolecules 52 (2019) 7386–7395.
[23] R. Yang, K. Zhang, Design and synthesis of flavonoid-based mono-, Bis-, and tri-Benzoxazines: toward elucidating roles of Oxazine ring number and hydrogen bonding on their polymerization mechanisms and thermal properties, Macromolecules 58 (2025) 616–626.
[24] S. Mukherjee, B. Lochab, Hydrogen bonding-guided strategies for thermal performance modulation in biobased oxazine ring substituted benzoxazine thermosets, Macromolecules 57 (2024) 1795–1807.
[25] C.F. Wang, S.F. Chiou, F.H. Ko, J.K. Chen, C.T. Chou, C.F. Huang, S.W. Kuo, F. C. Chang, Polybenzoxazine as a Mold-release agent for nanoimprint lithography, Langmuir 23 (2007) 5868–5871.
[26] M.G. Mohamed, M.M. Samy, T.H. Mansoure, S.U. Sharma, M.S. Tsai, J.H. Chen, J. T. Lee, S.W. Kuo, Dispersions of 1,3,4-Oxadiazole-linked conjugated microporous polymers with carbon nanotubes as a high-performance electrode for supercapacitors, ACS Appl. Energy Mater. 5 (2022) 3677–3688.
[27] M.M. Samy, I.M.A. Mekhemer, M.G. Mohamed, M.H. Elsayed, K.H. Lin, Y.K. Chen, T.L. Wu, H.H. Chou, S.W. Kuo, Conjugated microporous polymers incorporating Thiazolo[5,4-d]thiazole moieties for sunlight-driven hydrogen production from water, Chem. Eng. J. 446 (2022) 137158.
[28] Y. Zhu, P. Xu, X. Zhang, D. Wu, Emerging porous organic polymers for biomedical applications, Chem. Soc. Rev. 51 (2022) 1377–1414.
[29] J.S.M. Lee, M.E. Briggs, T. Hasell, A.I. Cooper, Hyperporous carbons from Hypercrosslinked polymers, Adv. Mater. 28 (2016) 9804–9810.
[30] M.G. Mohamed, A.F.M. EL-Mahdy, M.G. Kotp, S.W. Kuo, Advances in porous organic polymers: syntheses, structures, and diverse applications, Mater. Adv. 3 (2022) 707–733.
[31] W.T. Chung, I.M.A. Mekhemer, M.G. Mohamed, A.M. Elewa, A.F.M. EL-Mahdy, H. H. Chou, S.W. Kuo, K.C.W. Wu, Recent advances in metal/covalent organic frameworks based materials: their synthesis, structure design and potential applications for hydrogen production, Coord. Chem. Rev. 483 (2023) 215066.
[32] M.G. Mohamed, M.H. Elsayed, C.J. Li, A.E. Hassan, I.M.A. Mekhemer, A.F. Musa, M.K. Hussien, L.C. Chen, K.H. Chen, H.H. Chou, S.W. Kuo, Reticular design and alkyne bridge engineering in donor–π–acceptor type conjugated microporous polymers for boosting photocatalytic hydrogen evolution, J. Mater. Chem. A 12 (2024) 7693–7710.
[33] A. Basit, M.G. Mohamed, S.U. Sharma, S.W. Kuo, Thianthrene- and Thianthrene Tetraoxide-functionalized conjugated microporous polymers for efficient energy storage, ACS Appl. Polym. Mater. 6 (2024) 12247–12260.
[34] I.M.A. Mekhemer, A.M. Elewa, M.M. Elsenety, M.M. Samy, M.G. Mohamed, A. F. Musa, T.F. Huang, T.C. Wei, S.W. Kuo, B.H. Chen, S.D. Yang, H.H. Chou, Self-condensation for enhancing the hydrophilicity of covalent organic polymers and photocatalytic hydrogen generation with unprecedented apparent quantum yield up to 500 nm, Chem. Eng. J. 497 (2024) 154280.
[35] C.W. Hsiao, A.M. Elewa, M.G. Mohamed, M.G. Kotp, M.M.C. Chou, S.W. Kuo, Designing strategically functionalized hybrid porous polymers with octavinylsilsesquioxane/dibenzo[g,p]chrysene/benzo[c]-1,2,5-thiadiazole units for rapid removal of Rhodamine B dye from water, Colloids Surf. A Physicochem. Eng. Asp. 699 (2024) 134658.
[36] P.J. Waller, S.J. Lyle, T.M.O. Popp, C.S. Diercks, J.A. Reimer, O.M. Yaghi, Chemical conversion of linkages in covalent organic frameworks, J. Am. Chem. Soc. 138 (2016) 15519–15522.
[37] M.G. Mohamed, A. Basit, M. Madhu, K. Aravinthkumar, A.I. Said, D. Manoj, W. L. Tseng, S.W. Kuo, Conjugated Microporous Polymer Containing Pyrene and Dibenzo[g,p]chrysene Moieties as A Luminescent Powerhouse for Multi-Target Sensing and Environmental Safety, Microporous Mesoporous Mater 391 (2025) 113620.
[38] M.G. Mohamed, C.C. Chen, K. Zhang, S.W. Kuo, Construction of three-dimensional porous organic polymers with enhanced CO_2 uptake performance via solid-state thermal conversion from tetrahedral Benzoxazine-linked precursor, Eur. Polym. J. 200 (2023) 112551.
[39] H.R. Abuzeid, A.F.M. El-Mahdy, M.M.M. Ahmed, S.W. Kuo, Triazine-functionalized covalent Benzoxazine framework for direct synthesis of N-doped microporous carbon, Polym. Chem. 10 (2019) 6010–6020.
[40] S.J. Lyle, T.M.O. Popp, P.J. Waller, X. Pei, J.A. Reimer, O.M. Yaghi, Multistep solid-state organic synthesis of carbamate-linked covalent organic frameworks, J. Am. Chem. Soc. 141 (2019) 11253–11258.
[41] Q. Ma, X. Liu, H. Wang, Q. Zhuang, J. Qian, Construction of novel benzoxazine-linked covalent organic framework with antimicrobial activity via postsynthetic cyclization, Mater. Today Chem. 23 (2022) 100707.
[42] M.G. Mohamed, T.C. Chen, S.W. Kuo, Solid-state chemical transformations to enhance gas capture in Benzoxazine-linked conjugated microporous polymers, Macromolecules 54 (2021) 5866–5877.
[43] M.G. Mohamed, M.M. Samy, T.H. Mansoure, C.J. Li, W.C. Li, J.H. Chen, K. Zhang, S.W. Kuo, Microporous carbon and carbon/metal composite materials derived from bio-Benzoxazine-linked precursor for CO_2 capture and energy storage applications, Int. J. Mol. Sci. 23 (2022) 347.
[44] M. Ejaz, M.G. Mohamed, S.W. Kuo, Solid-state chemical transformation provides a fully benzoxazine-linked porous organic polymer displaying enhanced CO_2 capture and supercapacitor performance, Polym. Chem. 14 (2023) 2494–2509.
[45] M.M. Samy, M.G. Mohamed, T.H. Mansoure, T.S. Meng, M.A.R. Khan, C.C. Liaw, S. W. Kuo, Solid state chemical transformations through ring-opening polymerization of ferrocene-based conjugated microporous polymers in host–guest complexes with benzoxazine-linked cyclodextrin, J. Taiwan Inst. Chem. Eng. 132 (2022) 104110.
[46] M.G. Mohamed, W.C. Chang, S.W. Kuo, Crown ether- and Benzoxazine-linked porous organic polymers displaying enhanced metal ion and CO_2 capture through solid-state chemical transformation, Macromolecules 55 (2022) 7879–7892.
[47] H. Zhang, J. Guo, L. Liu, Z. Yu, N. Wei, Thiadiazole-functionalized Pb(ii)-MOF for "turn-on" fluorescence selective sensing of Al^{3+}, Cryst. Eng. Comm. 27 (2025) 956–963.
[48] S.L. Yao, R.H. Wu, P. Wen, H. Liu, T. Tu, S.J. Liu, A Zn(II) metal−organic framework with organic fluorescent ligands and hydrogen-bonding network for

effectively sensing Al^{3+} and Ga^{3+} ions, and proton conduction, Int. J. Mol. Struct. 1297 (2024) 136925.
[49] Z. Zhang, Z. Wu, Z. Li, Y. Zhao, M. Yu, F. Jiang, L. Chen, M. Hong, Stable In(III)-Based Metal–Organic Frameworks for Selective Detection of 4-Nitroaniline and Antibiotics in Water, Cryst. Growth Des. 23 (2023) 4491–4498.
[50] Y. Li, D.G. Cai, Z.H. Zhu, H. Xu, T.F. Zheng, J.L. Chen, S.J. Liu, H.R. Wen, Solvothermal synthesis and device fabrication of a Eu^{3+}-based metal–organic framework as a turn-on and blue-shift fluorescence sensor toward Cr^{3+}, Al^{3+} and Ga^{3+}, Dalton Trans. 52 (2023) 4167–4175.
[51] M.G. Mohamed, T.H. Mansoure, M.M. Samy, Y. Takashi, A.A.K. Mohammed, T. Ahamad, S.M. Alshehri, J. Kim, B.M. Matsagar, K.C.W. Kevin, S.W. Kuo, Ultrastable conjugated microporous polymers containing Benzobisthiadiazole and pyrene building blocks for energy storage applications, Molecules 27 (2022) 2025.
[52] C. Wang, W. Lu, W. Song, Z. Zhang, C. Xie, Y. Li, J. Wang, Highly crystalline benzothiadiazole covalent organic framework for enhanced Cr(VI) photocatalytic reduction by constructing donor-acceptor structure, Appl. Catal. B: Environ. Energy 361 (2025) 124583.
[53] S.Y. Chang, A.M. Elewa, M.G. Mohamed, I.M.A. Mekhemer, M.M. Samy, K. Zhang, H.H. Chou, S.W. Kuo, Rational design and synthesis of bifunctional Dibenzo[g,p]chrysene-based conjugated microporous polymers for energy storage and visible light-driven photocatalytic hydrogen evolution, Mater. Today Chem. 33 (2023) 101680.
[54] T.H. Weng, M.G. Mohamed, S.U. Sharma, I.M.A. Mekhemer, H.H. Chou, S.W. Kuo, Rationally engineered Ultrastable three-dimensional (3D) conjugated microporous polymers containing Triptycene, Tetraphenylethene, and Benzothiadiazole units as exceptional high-performance organic electrodes for supercapacitors, ACS Appl. Energy Mater. 6 (2023) 9012–9024.
[55] J. Wu, M.G. Mohamed, S.W. Kuo, Directly synthesized nitrogen-doped microporous carbons from polybenzoxazine resins for carbon dioxide capture, Polym. Chem. 8 (2017) 5481–5489.
[56] J. Jiang, M. Wang, W. Zhao, H. Liu, Y. Wang, P. Song, Z., Wang hierarchical porous carbon materials derived from N, O, S-containing bio-based polybenzoxazine for supercapacitors, Eur. Polym. J. 191 (2023) 112054.
[57] X. Sun, C. Wang, Y. Gong, L. Gu, Q. Chen, Y. Yu, A flexible sulfur-enriched nitrogen doped multichannel hollow carbon nanofibers film for high performance sodium storage, Small 14 (2018) 1802218.
[58] M.G. Mohamed, B.X. Su, S.W. Kuo, Robust nitrogen-doped microporous carbon via crown ether-functionalized Benzoxazine-linked porous organic polymers for enhanced CO_2 adsorption and supercapacitor applications, ACS Appl. Mater. Interfaces 16 (2024) 40858–40872.
[59] L. Sun, H. Zhou, L. Li, Y. Yao, H. Qu, C. Zhang, S. Liu, Y. Zhou, Double soft-template synthesis of nitrogen/sulfur-codoped hierarchically porous carbon materials derived from protic ionic liquid for supercapacitor, ACS Appl. Mater. Interfaces 9 (2017) 26088–26095.
[60] L. Ji, B. Wang, Y. Yu, N. Wang, J. Zhao, N, S co-doped biomass derived carbon with sheet-like microstructures for supercapacitors, Electrochim. Acta 331 (2020) 135348.
[61] S. Deng, T. Chen, T. Zhao, X. Yao, B. Wang, J. Huang, Y. Wang, G. Yu, Role of micropores and nitrogen-containing groups in CO_2 adsorption on indole-3-butyric acid potassium derived carbons, Chem. Eng. J. 286 (2016) 98–105.
[62] S.S. Shah, S.M. Abu Nayem, N. Sultana, A.J.S. Ahammad, M.A. Aziz, Preparation of sulfur-doped carbon for supercapacitor applications: a review, ChemSusChem 15 (2022) e202101282.
[63] G. Singh, R. Bahadur, A.M. Ruban, J.M. Davidraj, D.W. Su, A. Vinu, Synthesis of functionalized nanoporous biocarbons with high surface area for CO_2 capture and supercapacitor applications, Green Chem. 23 (2021) 5571–5583.
[64] S.V. Chaganti, S.U. Sharma, M. Ibrahim, A. Basit, P.N. Singh, S.W. Kuo, M. G. Mohamed, Redox-active a pyrene-4,5,9,10-tetraone and thienyltriazine-based conjugated microporous polymers for boosting faradaic supercapacitor energy storage, J. Power Sources 627 (2025) 235848.
[65] A. Basit, M.G. Mohamed, M. Ejaz, B.X. Su, H. Manzoor, S.W. Kuo, Boosting supercapacitor energy storage using microporous carbon derived from an Octavinylsilsesquioxane and Fluorenone-linked porous hybrid polymer, ACS Appl. Energy Mater. 7 (2024) 7505–7516.
[66] A. Wang, W. Xu, Y.J. Sun, K. Sun, J.C. Jiang, Heterogeneous activated carbon with graphitized shell and hydrophilic pores integrating high conductivity and pore affinity for excellent rate performance supercapacitors, Fuel 310 (2022) 122410.
[67] J.S.M. Lee, M.E. Briggs, C.C. Hu, A.I. Cooper, Controlling electric double-layer capacitance and pseudocapacitance in heteroatom-doped carbons derived from hypercrosslinked microporous polymers, Nano Energy 46 (2018) 277–289.
[68] M.G. Mohamed, S.U. Sharma, P.T. Wang, M. Ibrahim, M.H. Lin, C.L. Liu, M. Ejaz, H.J. Ye, S.W. Kuo, Construction of fully π-conjugated, diyne-linked conjugated microporous polymers based on tetraphenylethene and dibenzo[g,p]chrysene units for energy storage, Polym. Chem. 15 (2024) 2827–2839.
[69] A. Basit, Y.C. Kao, Y.A. El-Ossaily, S.W. Kuo, M.G. Mohamed, Rational engineering and synthesis of pyrene and thiazolo[5,4-d]thiazole-functionalized conjugated microporous polymers for efficient supercapacitor energy storage, J. Mater. Chem. A 12 (2024) 30508–30521.
[70] M.G. Mohamed, C.C. Chen, M. Ibrahim, A.O. Mousa, M.H. Elsayed, Y. Ye, S.W. Kuo, Tetraphenylanthraquinone and Dihydroxybenzene-tethered conjugated microporous polymer for enhanced CO_2 uptake and Supercapacitive energy storage, JACS Au 4 (2024) 3593–3605.